

NASA/TM—2018–219854



Understanding Friction Stir Welding

A.C. Nunes, Jr.

Marshall Space Flight Center, Huntsville, Alabama

March 2018

The NASA STI Program...in Profile

Since its founding, NASA has been dedicated to the advancement of aeronautics and space science. The NASA Scientific and Technical Information (STI) Program Office plays a key part in helping NASA maintain this important role.

The NASA STI Program Office is operated by Langley Research Center, the lead center for NASA's scientific and technical information. The NASA STI Program Office provides access to the NASA STI Database, the largest collection of aeronautical and space science STI in the world. The Program Office is also NASA's institutional mechanism for disseminating the results of its research and development activities. These results are published by NASA in the NASA STI Report Series, which includes the following report types:

- **TECHNICAL PUBLICATION.** Reports of completed research or a major significant phase of research that present the results of NASA programs and include extensive data or theoretical analysis. Includes compilations of significant scientific and technical data and information deemed to be of continuing reference value. NASA's counterpart of peer-reviewed formal professional papers but has less stringent limitations on manuscript length and extent of graphic presentations.
- **TECHNICAL MEMORANDUM.** Scientific and technical findings that are preliminary or of specialized interest, e.g., quick release reports, working papers, and bibliographies that contain minimal annotation. Does not contain extensive analysis.
- **CONTRACTOR REPORT.** Scientific and technical findings by NASA-sponsored contractors and grantees.
- **CONFERENCE PUBLICATION.** Collected papers from scientific and technical conferences, symposia, seminars, or other meetings sponsored or cosponsored by NASA.
- **SPECIAL PUBLICATION.** Scientific, technical, or historical information from NASA programs, projects, and mission, often concerned with subjects having substantial public interest.
- **TECHNICAL TRANSLATION.** English-language translations of foreign scientific and technical material pertinent to NASA's mission.

Specialized services that complement the STI Program Office's diverse offerings include creating custom thesauri, building customized databases, organizing and publishing research results...even providing videos.

For more information about the NASA STI Program Office, see the following:

- Access the NASA STI program home page at <<http://www.sti.nasa.gov>>
- E-mail your question via the Internet to <help@sti.nasa.gov>
- Phone the NASA STI Help Desk at 757-864-9658
- Write to:
NASA STI Information Desk
Mail Stop 148
NASA Langley Research Center
Hampton, VA 23681-2199, USA

NASA/TM—2018–219854



Understanding Friction Stir Welding

A.C. Nunes, Jr.

Marshall Space Flight Center, Huntsville, Alabama

National Aeronautics and
Space Administration

Marshall Space Flight Center • Huntsville, Alabama 35812

March 2018

Acknowledgments

The author gratefully acknowledges the contributions of the many collaborators to this Technical Memorandum (TM): management, engineers, contractors, and technicians from NASA Marshall Space Flight Center (MSFC), Materials and Processes Laboratory; participants in the Summer Faculty Research Fellowship program and the Graduate Student Research program; and colleagues in the world at large. Engineer R. Jeff Ding brought friction stir welding (FSW) to MSFC in the mid 1990's. The author began his studies of FSW as a weld process analyst at this time. By 2000, Branch Chief Carolyn K. Russell ordered him down to the Michoud Assembly Facility to defend his new wiping model of the FSW process in an internal Independent Research and Development review in opposition to an extrusion model prevailing at the time. At the instigation of Anthony P. Reynolds of the University of South Carolina (USC), he presented the wiping model at the 37th Annual Technical Meeting of the Society for Engineering Science, Inc. the same year at USC. This was the beginning of a lengthy, not yet completed development of the FSW model presented in this TM. The principal collaborator in the early development phases was John C. McClure of the University of El Paso. In the later development phase, Judith A. Schneider, originally of Mississippi State University, now of The University of Alabama—Huntsville took over this role. Drs. McClure and Schneider both served as summer faculty and both set up their own FSW laboratories. Dr. Schneider, in addition, spent a year at MSFC on an Intergovernmental Personnel Act assignment. Among the many laboratory personnel who contributed to the study were Robert Carter (2001) and Zachary S. Courtright (2016) of the MSFC laboratory. They contributed the data used in the examples presented in this TM.

TRADEMARKS

Trade names and trademarks are used in this report for identification only. This usage does not constitute an official endorsement, either expressed or implied, by the National Aeronautics and Space Administration.

Available from:

NASA STI Information Desk
Mail Stop 148
NASA Langley Research Center
Hampton, VA 23681-2199, USA
757-864-9658

This report is also available in electronic form at
<<http://www.sti.nasa.gov>>

TABLE OF CONTENTS

1. INTRODUCTION	1
2. DECOMPOSING THE FRICTION STIR WELDING FLOW FIELD	5
2.1 The Difference Between Plastic Metals and Viscous Fluids: The Shear Surface	5
2.2 Tool Rotation Effects: The Rotating Plug Component Field	6
2.3 Tool Rotation Plus Translation Effects: Superposing a Uniform Flow Component Field	9
2.4 Tool Geometry Effects: The Ring Vortex Flow Component Field	12
2.5 Tool Eccentricity Effects: Oscillations	15
2.6 Summary: The Interpretation of Friction Stir Weld Structures	18
3. TEMPERATURES IN FRICTION STIR WELDING	21
3.1 Temperature Variation Over the Shear Surface (Part 1)	21
3.2 Flow Stress Dependence on Strain Rate and Temperature	24
3.3 Temperature Variation Over the Shear Surface (Part 2)	25
4. TORQUES AND FORCES IN FRICTION STIR WELDING	29
4.1 Torque	30
4.2 Steady Tool Forces (Part 1)	31
4.3 Pressure Variation on Shear Surface	32
4.4 Steady Tool Forces (Part 2)	33
4.5 The Shape of the Shear Surface	34
4.6 Torque, Drag, and Lateral Forces	35
4.7 Sample Computations: Torque, Drag, and Lateral Force	36
4.8 Force Variations	42
4.9 Force Oscillations	42
5. SUMMARY	46
APPENDIX A—SHEAR SURFACE WIDTH	48
APPENDIX B—SHEAR SURFACE POSITION	53
APPENDIX C—LATERAL CONTOUR OF ISOTHERMAL SHEAR SURFACE	55

TABLE OF CONTENTS (Continued)

APPENDIX D—COMPARISON OF COMPUTATIONS WITH MEASURED FORCES	58
REFERENCES	60

LIST OF FIGURES

1.	Plan section of a friction stir weld about half way down the pin. The weld (220 RPM, 3.5 in/min in 0.317-in-thick, 2219-T87 aluminum alloy) was suddenly stopped and the pin cavity filled with mounting medium (exhibiting bubbles). The shear surface separating flow rotating with the tool from the bulk weld metal is shown by a dashed line. The rotating metal bulges on the retreating side to accommodate the backflow of metal from the leading to the trailing edge of the pin	2
2.	Sketch of interface between tool and weld metal. Given sufficient pressure, the weld metal sticks to the tool except at the edge of the shoulder where the pressure drops off to zero. The shearing interval collapses to a shear surface, which, with the sticking surface at the tool, bounds a plug of weld metal rotating with the tool	8
3.	Streamlines in superposed rotating plug and uniform flow fields. Compare with figure 1. The advancing side streamline circumscribes a rotating eddy shown darkened. As there is no flow perpendicular to a streamline, no flow enters or leaves the eddy, which can be replaced by the friction stir pin	11
4.	The trace of the weld seam takes a ‘lazy S’ shape (or sometimes a ‘zigzag’ shape) in a conventional friction stir weld due to the action of the ring vortex flow field component	13
5.	Plan views of bimetallic FSW weld: (a) Basic division of flows—metal on the retreating side flows over that on the advancing side. Alterations in contrast due to grain refinement are not shown. Complications arise due to the ring-vortex circulation (lateral displacement of the seam trace), oscillations (a wavy seam trace), or significant differences in flow stress (complex) and (b) 2219 aluminum alloy (advancing side) versus 2195 aluminum alloy (retreating side) (courtesy of G. Bjorkman, Lockheed Martin)	14
6.	Flow arms, where the parent metal apparently penetrates into refined nugget material, are seen where the outward radial component of the translational flow is less than the inward radial component of the ring vortex circulation	15
7.	Ripple contours: $R = 0.250$ in, $R_S = 0.600$ in, $w = 0.315$ in, 220 RPM, 6 in/min, position control	16

LIST OF FIGURES (Continued)

8.	Longitudinal section of a partial penetration friction stir weld cavity in 2219 aluminum alloy (400 RPM, 2 in/min, 3° lead angle, 0.5–20 NF thread, courtesy of J.C. McClure). Internal bands and ripples can be seen emerging from the trailing edge of the shear surface. The bands are distorted in the ring vortex circulation	17
9.	Transverse weld: (a) Schematic synthesis of features due to various FSW flow components on transverse weld section and (b) transverse bead-on-plate section in 0.5-in-thick, 2219 aluminum alloy (400 RPM, 2 in/min, 3° lead angle, courtesy of J.C. McClure)	19
10.	Subdivision of the volume outside the FSW shear surface into slices of thickness, dz , and the slices into sectors of angle, $d\theta$. Heat is taken to flow from the shear surface through each sector independently to radius, R_o , at ambient temperature, T_o	22
11.	Estimate of flow stress temperature dependence from typical ultimate tensile strength versus temperature data in ASM Metals Handbook. Flow stress is assumed proportional to the ultimate tensile strength. The linear approximation $\tau = \left(-\frac{\partial\tau}{\partial T}\right)(T_{\text{melt}} - T)$, where $\left(-\frac{\partial\tau}{\partial T}\right) \approx \frac{0.2 \tau_{\text{max}}}{T_{\text{melt}}} \sim 5.9 \frac{\text{psi}}{\text{°K}}$, holds down to around $0.75 T_{\text{melt}} \approx 340 \text{ °C}$ and encompasses the anticipated range of FSW temperatures	25
12.	Local pressure, P , and shear, τ , on shear surface determine the tool forces	32
13.	Weld metal entry into the circumferential flow around the tool is held back until the dynamic pressure, P_{dyn} , is large enough to overcome the local shear stress resistance to turning from radial to circumferential flow	33
14.	Simplified flared cylindrical shear surface with radius, $r(z)$ and flat bottom	35
15.	Example 1 comparison of computation and measurement for 0.5-in-diameter pin and 1.2-in-diameter shoulder in 2219-T87 aluminum alloy for 8 in/min and 150 to 270 RPM: (a) Torque shows agreement in trend and magnitude, (b) drag shows agreement in trend, but computation overestimates drag, and (c) lateral force computation overestimates force and shows trend opposite to measurement	38

LIST OF FIGURES (Continued)

16.	Example 2 comparison of computation and measurement for 0.19-in-diameter pin and 0.48-in-diameter shoulder in 2219-T87 aluminum alloy for 4 to 15 in/min and 800 to 3,000 RPM: (a) Torque shows agreement in trend and magnitude, (b) drag shows agreement in trend, but computation underestimates drag, and (c) lateral force computation is of similar magnitude to measurements, but measurements are erratic, even reversing sign, and do not show a definite trend for comparison	40
17.	Torque and plunge force variation with position of tool along weld in 0.327-in-thick, 2195-T81 aluminum alloy. Vertical lines mark 1.5-in-wide gaps between 4.5-in-wide clamps. Welds were made at 200 RPM and 6 in/min. A 0.311-in-long, 1/2-20 UNJF threaded pin was used with a smooth 1.2-in-diameter shoulder	42
18.	Drag or plow force variation with position of tool along weld in 0.327-in-thick, 2219-T87 aluminum alloy. From top to bottom, each curve represents a weld made at a different preweld eccentricity: 0.0004 in, 0.0013 in, 0.0023 in, 0.0045 in, and 0.0110 in. Welds were made at 220 RPM and 6 in/min with a 2.5° lead angle. A 1/2-20 UNJF threaded pin was used with a smooth 1.2-in-diameter shoulder	43
19.	Tool preweld eccentricity effect: (a) Drag or plow force variation and (b) lateral or side force variation with tool eccentricity. Variations appear roughly the same, suggesting a force rotating with the tool	44
20.	A simplified model of the shear surface comprising a shearing column of metal extended in the y -direction with the bottom at $y=0$ fixed and the top made to move at velocity V	48
21.	A simplified model of the shear surface comprising a shearing column of metal extended in the y -direction with the bottom at $y=0$ fixed and the top made to move at velocity, V . The shear surface is located between $y=s$ and $y=s+\delta$. The location of the shear surface, s , depends upon the boundary conditions at $y=0$ and $y=w$	53
22.	Approximate shear surface lateral contour from simplified computation. Compare with apparent contours of figure 21	56

LIST OF TABLES

1.	Structural features related to flow components	18
2.	Flow field components related to controlling factors	20
3.	Comparison of estimated and measured oscillation amplitudes of drag and lateral forces	44
4.	Latent eccentricity that, added to measured tool eccentricity, would bring force oscillation estimates equal to measurement	45
5.	Various estimates of the shear surface contour for pin radius, $R=0.25$ in; shoulder radius, $R_s=0.75$ in; and pin length, $w=0.25$ in	56
6.	Comparison of computations with measured forces—example 1	58
7.	Comparison of computations with measured forces—example 2	59

LIST OF ACRONYMS AND ABBREVIATIONS

FSW	friction stir welding
IPM	inches per minute
MSFC	Marshall Space Flight Center
RPM	revolutions per minute

NOMENCLATURE

C	specific heat
E	activation energy
h	height
$\hat{i}, \hat{j}, \hat{k}$	unit vectors in x, y, z directions, respectively
k	thermal conductivity
κ	Boltzmann's constant
M	torque
n	dimensionless parameter used in mathematical expression representing shear surface shape
P	pressure
P_{dyn}	dynamic pressure
P_{stat}	static pressure
Q_{cond}	power loss from the shear surface through conduction to the environment
Q_{conv}	power loss from the shear surface through convection, i.e., to heat metal entering the shear surface
Q_{gen}	power generated at the shear surface through plastic deformation
R	radius of shear surface
R_o	radius at which ambient temperature is reached to sufficiently close approximation to be used to estimate conduction losses
R_s	radius of tool shoulder
r	polar coordinate about tool; radius from tool axis

NOMENCLATURE (Continued)

s	location of shear surface
T	absolute temperature
$T(0)$	pin temperature
T_o	ambient temperature
$T(w)$	anvil temperature
u	metal flow velocity in simplified shear surface model
V	weld speed, velocity
\vec{V}_1, \vec{V}_2	flow velocity fields
V_x, V_y, V_z	flow velocity field components in x, y, z directions, respectively
v	radially inward velocity component
v	activation volume
w	pin length
x	coordinate from tool center in direction of weld motion
y	coordinate from tool center in plane of weld metal plate toward retreating side of tool, also lateral displacement of streamline from tool centerline toward retreating side of tool
y_o	initial lateral displacement of streamline from tool centerline toward retreating side of tool as it meets the shear surface
z	coordinate from tool bottom perpendicular to plane of weld metal plate toward tool spindle
β	coefficient of friction
$\dot{\gamma}$	shear deformation rate

NOMENCLATURE (Continued)

$\dot{\gamma}_0$	unimpeded shear deformation rate
δ	shear surface width; ripple height
ε	eccentricity of tool axis with respect to shear surface axis
ζ	integration variable
θ	angle from direction of weld motion toward retreating side of tool
θ_0	angular coordinate at which streamline meets shear surface
ν	constant of proportionality
ρ	weld metal density
τ	shear flow stress
ϕ	lead angle of tool axis
φ	phase angle
ω	angular velocity of FSW tool

TECHNICAL MEMORANDUM

UNDERSTANDING FRICTION STIR WELDING

1. INTRODUCTION

In the friction stir welding (FSW) process, a rotating threaded pin seized in a weld seam is moved along the seam, stirring the sides of the seam together into a weld as it goes. A shoulder prevents upflow of metal around the pin, which would result in plowing rather than welding. Friction stir welds are strong and reliable and are increasingly used in the aerospace industry in general and by NASA in particular.

The FSW process was invented¹ at The Welding Institute, Cambridge, UK, in 1991. It was taken up by the Materials and Processes Laboratory at NASA Marshall Space Flight Center (MSFC) in 1995 as a means to circumvent fusion welding problems with a new aluminum alloy. The process was developed initially by empirical methods. The details of the metal flow around the FSW tool are complex and, still after more than two decades since the process was invented, are not well understood.

Researchers seeking to understand the FSW process put forth various models. At the time when MSFC began to study the FSW process, two models predominated: (1) The extrusion model, where the tool was conceived as heating the surrounding metal by friction and moving forward as the heat-softened metal was extruded back past the pin, and (2) the fluid model, where the weld metal was treated as a viscous fluid. Neither model represented the FSW process very well. They did not explain most weld structural features, and ad hoc parameters, friction coefficients or viscosities, were required to estimate welding torques or forces.

By the year 2000, MSFC was presenting a wiping model, where the weld metal was conceived to be wiped onto the FSW tool, carried around the tool, and wiped off onto the tool wake. This was an early form of an FSW process model that does explain weld structure and that also offers a means for estimating the temperatures, torques, and forces occurring during the welding process. The key to the MSFC model is the recognition of the role played by the shear surface, a plastic instability called an ‘adiabatic shear band,’ as the principal shear deformation site for the FSW deformation process. (The shear surface is analogous to the shear plane that separates chip and workpiece in metal cutting process models.) The shear surface separates a plug of metal sticking to the tool from the weld metal surrounding the tool. The shear surface enables a great simplification in modeling the FSW process and is the foundation for the innovations presented in this Technical Memorandum.

Given the shear surface, it is possible to decompose the metal flow field in the vicinity of the tool into a few relatively simple component fields, each field satisfying independently a particular set of boundary conditions. Flow streamlines can be estimated from combined component fields and confirmed by tracer experiments.^{2,3} Flow features like the ‘lazy-S’ shape of the trace of the weld seam can be estimated from streamline lateral displacements. Perturbations of weld structure by changes in tool geometry⁴ can be estimated through addition of appropriate flow field components. The thickness of the eccentric bulge of the shear surface on the retreating side of the tool, where the weld metal flows (or is wiped) from front to back of the tool as the tool progresses, can be estimated and observed (fig. 1). It is possible to interpret and understand the structure of friction stir welds using flow components in a manner analogous to the interpretation of fusion weld structure using phase diagrams.

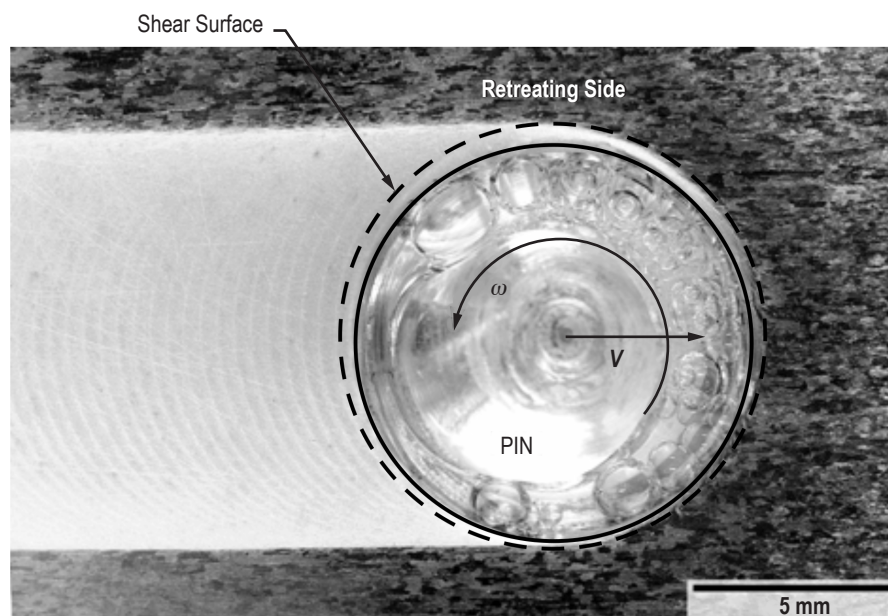


Figure 1. Plan section of a friction stir weld about half way down the pin. The weld (220 RPM, 3.5 in/min in 0.317-in-thick, 2219-T87 aluminum alloy) was suddenly stopped and the pin cavity filled with mounting medium (exhibiting bubbles). The shear surface separating flow rotating with the tool from the bulk weld metal is shown by a dashed line. The rotating metal bulges on the retreating side to accommodate the backflow of metal from the leading to the trailing edge of the pin.

Given the restriction of heat input to the shear surface, where the main deformation occurs, a relatively simple heat balance to determine the weld (shear surface) temperature can be set up. Heat losses to conduction or to convection (to heat cooler metal as it approaches the tool) balance mechanical energy input. The mechanical input depends upon the imposed shear rate and the flow stress of the weld metal.

The flow stress of a metal depends upon temperature, strain rate, and past history of deformation. The temperature dependence is strong. It can be linearized over the FSW temperature range. The strain rate dependence is weak, as is characteristic of metals, but not viscous materials. The tendency of metals toward adiabatic shear bands is a result of the weak dependence of the flow stress on strain rate. In viscous materials, the decrease in stress at a given location due to a temperature rise can be countered by a modest rise in strain rate so as to maintain a continuous strain rate distribution. In metals with very little shear stress dependence on strain rate, extremely high strain rates are required to balance a local drop in stress as the temperature rises. Hence, the region where deformation occurs narrows into an adiabatic shear band, i.e., a shear surface. At FSW temperatures, the properties of the metal tend to be structure insensitive due to the rapidity of diffusion processes so that a simplified constitutive relation may be used. Thus, a complexity that would require finite element computation techniques can be avoided, and results may be obtained in simple analytical form.

The heat balance depends upon both flow stress and temperature. Flow stress depends upon temperature. The two relations can be solved for either flow stress or temperature. The torque can be computed directly from the flow stress. In the two empirical examples used to check the FSW model, the computed torques showed good agreement with empirical data (fig. 15(a) in sec. 4.7.1 and fig. 16(a) in sec. 4.7.2).

The temperature at a specific location on the shear surface location can be estimated by splitting the conductive environment of the FSW tool into independent sectors. Greater mechanical power input or thermal convection input increases the shear surface temperature required to balance and conduct the heat away from each specific location. The temperature is slightly higher on the advancing side, where the strain rate is higher, and lower on the retreating side. The temperature is lower on the leading edge, where the convective heat loss to cooler incoming metal reduces the need for high temperatures to conduct away the mechanical power input, and hotter on the trailing edge. The hottest temperatures tend to occur on the advancing portion of the trailing edge of the shear surface. Measured temperature variations around the tool exhibit this kind of variation,⁵ but it should be kept in mind that the approximation on which the computation is based is crude, and the level of precision of the computations remains to be seen.

The drag is determined by the summation of pressure and shear forces acting on the shear surface. The shear stress depends upon the local temperature. The pressure has to be enough to force the radial inflow around a corner against shear stress opposition into the rotating flow around the pin, hence, it varies with the shear stress. The computed drag shows the same variation with parameters as the data for both empirical studies, but the computed drag magnitudes are 2 to 3 times greater than the empirical data for example 1 and roughly half the empirical data for example 2. This implies an unaccounted-for variable differing between the two examples.

The lateral force is also determined by the summation of pressure and shear forces acting on the shear surface, at least as far as the computations go. The computations fell very roughly into the same range as the data: 982 to 1,803 lb computed versus 418 to 1,012 lb measured for example 1, and 15 to 33 lb computed versus -10 to 20 lb measured for example 2. However, in example 1, while the computed force fell with revolutions per minute (RPM), the measured force rose.

In example 2, the lateral force showed too much scatter to determine a trend in variation with the weld speed divided by RPM, while the computed force uniformly rose. In two cases, the direction of the measured force reversed. This implies an unaccounted-for variable competing with the weld parameters. Interaction of the end of the tool with the anvil could have such an effect.

Self-reacting FSW configurations have not been discussed here, but as these configurations are almost like two conventional configurations back to back, the discussions should translate easily to self-reacting configurations.

2. DECOMPOSING THE FRICTION STIR WELDING FLOW FIELD

2.1 The Difference Between Plastic Metals and Viscous Fluids: The Shear Surface

That metals are not viscous fluids is obvious from the insensitivity of their flow stresses to strain rate.⁶ Sensitivity to flow stress is determined by the deformation mechanisms encountered in a medium. Flow in both viscous and plastic (metallic) media is thermally activated. The assistance of local elastic oscillations (heat) is needed to help the local structure pass over an ‘activation energy’ barrier, E , holding it back from the flow deformation. An applied shear stress, τ , partly overcomes the barrier, reducing it to $E - \tau v$, where the effect of τ is linearized for simplicity. The constant of proportionality, v , is called the ‘activation volume.’

Deformation takes place by a series of jumps across the barrier, each jump contributing a specific amount of deformation. The rate of deformation $\dot{\gamma}$ is proportional to the number of jump sites per unit volume and to the jump attempt frequency, the natural oscillation frequency at the site. These features vary with the material and its internal structural changes during deformation, but not with stress per se. Stress affects the deformation rate through the probability that a jump attempt will succeed. Such probabilities typically vary proportional to an exponential $e^{-\frac{E-\tau v}{\kappa T}}$ where κ is the Boltzmann’s constant and T is the absolute temperature.

Suppose a medium deforms by local rearrangements that can go either forward or back. Taking $\dot{\gamma}_o$ as the deformation rate in either forward or reverse direction if every jump were to succeed the flow rate becomes

$$\dot{\gamma} = \dot{\gamma}_o e^{-\frac{E-\tau v}{\kappa T}} - \dot{\gamma}_o e^{-\frac{E+\tau v}{\kappa T}} = \dot{\gamma}_o e^{-\frac{E}{\kappa T}} \left(e^{\frac{\tau v}{\kappa T}} - e^{-\frac{\tau v}{\kappa T}} \right) = 2\dot{\gamma}_o e^{-\frac{E}{\kappa T}} \sinh\left(\frac{\tau v}{\kappa T}\right). \quad (1)$$

If the effect of stress is appreciably smaller than the thermal fluctuations, i.e., $\tau v \ll \kappa T$, then $\sinh\left(\frac{\tau v}{\kappa T}\right) \approx \frac{\tau v}{\kappa T}$ and

$$\dot{\gamma} = 2\dot{\gamma}_o e^{-\frac{E}{\kappa T}} \left(\frac{\tau v}{\kappa T}\right) = \frac{2\dot{\gamma}_o v}{\kappa T} e^{-\frac{E}{\kappa T}} \tau. \quad (2)$$

The strain rate is proportional to the acting stress. This constitutes viscous behavior.

Metals typically (but not always) deform by a shearing process where shear is spread across slip planes through the motion of linear defects called ‘dislocations.’ Dislocations bow out against

pinning points. Reversals of jumps past pinning points are too improbable to be considered, hence

$$\dot{\gamma} = \dot{\gamma}_o e^{-\frac{E-\tau\nu}{\kappa T}} \quad (3)$$

Solving for the stress,

$$\tau = \frac{E}{\nu} - \frac{\kappa T}{\nu} \ln\left(\frac{\dot{\gamma}_o}{\dot{\gamma}}\right) \quad (4)$$

The flow stress is proportional to the logarithm of the strain rate, much less sensitive to strain rate than viscous behavior. This constitutes plastic behavior.

Comparison of idealized equations (2) and (4) illustrates how deformation mechanisms can affect sensitivity to strain rate. The parameters ν and $\dot{\gamma}_o$ in equation (4) are not, strictly speaking, constants but alter with strain and time. Real deformation mechanisms are complex. Given an imposed stress, a number of deformation mechanisms can operate at the same time. The flow stress temperature dependence exhibited in figure 11 in section 3.2 is a result of a succession of flow mechanisms. At higher temperatures, the structures introduced by deformation and heat treatment processes tend to be destroyed or dissolved. At FSW temperatures close to the tool, metals tend not to be sensitive to temperature conditions, but temperature-induced structures do not vanish instantaneously. Metal properties used here are approximations.

A consequence of the insensitivity of flow stress to strain rate is a tendency to inhomogeneous deformation, particularly at high strain rates.⁷ Inhomogeneous shear is often encountered in metal cutting and in FSW because of the insensitivity of metals to strain rate. A shear surface, analogous to the metal cutting shear plane, forms around the FSW tool and has a critical effect on the FSW flow field and weld structure.

In FSW, a relatively slow subsidiary flow takes place side by side with the rapid shear surface flow. Such subsidiary flow is not important when paralleled by a much faster flow like that at the shear surface, although its effects are clearly visible in distortions of the weld seam prior to encountering the shear surface. (These distortions might be used to estimate an effective viscosity of the weld metal.) Sometimes, however, when a slow, auxiliary deformation is not paralleled by a faster deformation mechanism, it is the main flow. This is the case for the ring vortex flow component discussed in section 2.4.

2.2 Tool Rotation Effects: The Rotating Plug Component Field

Whether the weld metal slips against or sticks to the tool surface depends upon the coefficient of friction and the surface pressure. Given a plunge force of 5,000 lb acting on a 1-in-diameter shoulder, a mean pressure under the shoulder of 6,366 psi results. Given a shear flow stress of the weld metal at FSW temperatures of 2,000 psi, a friction coefficient over 0.3 would prevent slippage. For clean, dry aluminum and steel, a friction coefficient conducive to sticking would be

anticipated. Pin threads and/or shoulder scrolls would raise the effective friction coefficient so as to ensure sticking, except at the very edge of the shoulder.

Slip must take place at the tool/weld metal interface, but shearing can occur anywhere in the weld metal. The shear surface is not constrained by the tool/workpiece interface but takes a shape that presumably minimizes the torque required to turn the tool. (Once rotation occurs, there is no reason for the torque to rise to a level that might excite more difficult modes of deformation.) The shear surface and the sticking surface together bound a plug of metal that rotates with the tool.

The trace of the FSW shear surface in a weld section is marked by a sudden structural change. This sudden change is visible and is labeled on the plan section of figure 1 and on the longitudinal section of figure 8 in section 2.5. The shear surface is commonly observed to encounter the sticking surface on the bottom of the shoulder, close to the edge of the shoulder. This shows that the weld metal sticks to almost the entire surface of the tool. It is probably safe to assume that the weld metal sticks to the tool surface over almost the entire contact surface. A little slippage is, of course, expected at the outer edge of the tool shoulder, where the pressure drops off. As slippage increases at the shoulder edge, the shear surface moves inward away from the edge.

If the weld metal sticks to the tool surface and rotates with it, and a short distance away from the tool the weld metal is not rotating, the metal in the interval between must be shearing. Imagine a thin ring element cut out of the shearing interval. The torque, M , on the ring between radius r_1 and r_2 is given as

$$M = 2\pi hr_2^2 \tau_2 - 2\pi hr_1^2 \tau_1 , \quad (5)$$

where h is the height and τ is the shear flow stress of the metal. If $r^2\tau$ changes from one side of the ring element to the other, the resultant net moment causes the ring element to accelerate. So $r^2\tau$ has to be constant within the flow around the tool if steady motion is to be preserved. As the radius, r , increases, the metal flow stress has to drop to preserve equilibrium.

There is a thermal equilibrium too that must be preserved given a steady-state process. The temperature gradient must be sufficient to conduct away the heat generated by the plastic deformation.

The shear stress of plastically deforming metal, i.e., the metal flow stress, depends upon temperature, T , and shear rate, $\dot{\gamma}$. The temperature and shearing rate can only adjust themselves to maintain plastic flow in a limited radial zone. If, as is the case for metals, the flow stress is not very sensitive to strain rate, shear rate adjustments to maintain equilibrium must be quite large and the drop in angular velocity at the shear zone must be very steep. Hence, the shear ‘surface’ between the rotating plug of metal attached to the tool and the weld metal clamped to the anvil is expected to be very narrow. The sharp transition between refined grain nugget material and the relatively coarse grained parent metal shown in figure 1 confirms this expectation.

In appendix A, the width of the shear zone is estimated for a simplified model, where a shearing velocity is applied to the top of a column with a fixed base. The width, δ , of the shear zone is estimated at

$$\delta = \frac{\pi}{2} \sqrt{\frac{k \left(\frac{\partial \ln \tau}{\partial \dot{\gamma}} \right)}{\left(-\frac{\partial \tau}{\partial T} \right)}}. \quad (6)$$

The shear zone width of equation (6) increases with thermal conductivity, k , and sensitivity of flow stress to strain rate $(\partial \ln \tau / \partial \dot{\gamma})$ and decreases with sensitivity of flow stress to temperature $(-\partial \tau / \partial T)$. If the weld metal flow stress were completely insensitive to strain rate, the shear zone would have zero width.

In figure 1, a large, sharp grain size change a little beyond the leading edge of the tool clearly marks the leading edge of the shear surface. The trailing edge is not so clearly marked as the refined grain size does not change a second time upon crossing the shear surface. Neither the large parent metal grains nor the refined grains in the wake of the tool appear to change significantly except at the shear surface, where the refinement takes place. Thus, the shear zone around the FSW tool appears to contract essentially to a surface, the ‘shear surface.’ The shear surface as illustrated in figure 2 takes the shape of a flared cylinder encapsulating the rotating plug of metal that sticks to the tool.

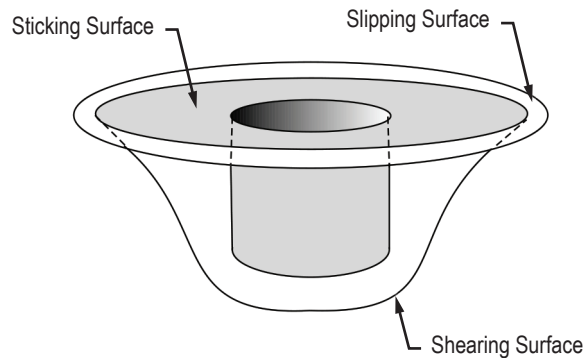


Figure 2. Sketch of interface between tool and weld metal. Given sufficient pressure, the weld metal sticks to the tool except at the edge of the shoulder where the pressure drops off to zero. The shearing interval collapses to a shear surface, which, with the sticking surface at the tool, bounds a plug of weld metal rotating with the tool.

What is happening at the shear surface? It is possible to imagine a dislocation model. Shear in metals takes place by the movement of linear defects called ‘dislocations.’ As the parent metal grains enter the shear surface, dislocation sources are activated and torrents of dislocations flow

across slip planes, which parallel the shear surface. Positive dislocations flow in one direction; negative dislocations flow in the opposite direction. Many positive-negative encounters result in annihilation and generation of elastic waves, i.e., heat. A few encounters result in tangles that form the basis of a new refined grain structure.

Whether or not the grain refinement process should be characterized as ‘dynamic recrystallization’ depends upon whether the new grains emerge directly out of the dislocation tangles or subsequently through a nucleation and growth process. A detailed dislocation model for the shear surface mechanism might allow an estimate of the refined grain size and the variation in grain size within the weld nugget. Grain size variations⁴ might be attributable to temperature differences⁵ on the shear surface.

Unlike a slipping surface, a shearing surface is not confined to the tool surface except at its boundaries. The shear surface takes the shape that makes it easiest to turn the FSW tool. (The weak link is where the chain breaks.) The flaring shape of the shear surface may be estimated by minimizing torque using the calculus of variations or other approximations. The general shape of a shear surface is sketched in figure 2.

2.3 Tool Rotation Plus Translation Effects: Superposing a Uniform Flow Component Field

Let us consider two simple flow fields: (1) A plug of metal rotating with angular velocity, ω , within a cylinder in a stationary environment, and (2) a uniform flow of metal with velocity, V . A superposition of a rotating plug flow field and a uniform flow field begins to model the flow field around a FSW tool. The rotating plug flow matches the boundary conditions at the tool rotating at angular velocity ω . The uniform flow matches the boundary conditions at the edge of the weld plate, which approaches the tool at weld speed V . It can be seen by inspection that the rotating plug and uniform flows do not affect changes in local density. These flow fields would be compatible with flow fields in metals, which deform by shearing but not appreciably by dilation. Metal flows are incompressible.

If the flow field around an FSW tool was represented by superposing incompressible flow fields V_1 and V_2 , would the combined flow field $V_1 + V_2$ still be incompressible?

For incompressibility the net volume flow rate in and out of every tiny element of volume must be zero. For a little cube with sides dx , dy , dz the volume influx through the $dydz$ face is $V_x dydz$, where V_x is the local x -component of the velocity field. The volume outflux on the other side of the cube is $V_x dydz + \frac{\partial V_x}{\partial x} dx dy dz$. Incompressibility would require that the flows in and out balance. Mathematically stated, that is

$$\frac{\partial V_x}{\partial x} + \frac{\partial V_y}{\partial y} + \frac{\partial V_z}{\partial z} = \left(\hat{i} \frac{\partial}{\partial x} + \hat{j} \frac{\partial}{\partial y} + \hat{k} \frac{\partial}{\partial z} \right) \cdot (V_x \hat{i} + V_y \hat{j} + V_z \hat{k}) = \nabla \cdot \vec{V} = 0, \quad (7)$$

where the expression is written in a couple of equivalent vector forms. This is a familiar equation from fluid mechanics, but it applies independently for incompressible flows whatever the medium.

It is a linear equation, that is

$$\nabla \cdot (\vec{V}_1 + \vec{V}_2) = \nabla \cdot \vec{V}_1 + \nabla \cdot \vec{V}_2 . \quad (8)$$

Hence, if two flows are incompressible, their superposition is also incompressible.

The superposition of a uniform flow field upon a rotating plug flow yields an incompressible flow field satisfying the boundary conditions of the weld metal, a rough model* of the flow around an FSW tool. The quality of the representation can be assessed by comparing computed macro-structural features with empirical observations. The quality of the representation can be improved by superimposing additional flow components.

Inside the rotating plug the flows combine to yield a radial velocity

$$\frac{dr}{dt} = -V \cos \theta \quad (9)$$

and an angular velocity

$$\frac{d\theta}{dt} = \omega + \frac{V}{r} \sin \theta , \quad (10)$$

where V is the weld speed and ω is the tool angular velocity.

These velocities can be combined to yield streamlines

$$dr = -\frac{V}{\omega} \frac{d \sin \theta}{1 + \frac{V}{r\omega} \sin \theta} \approx -\frac{V}{\omega} d \sin \theta , \quad (11)$$

which can be integrated to

$$r \approx R - \frac{V}{\omega} (\sin \theta - \sin \theta_o) , \quad (12)$$

* The classical approach to modeling would be to invoke equilibrium, constitutive, compatibility, and energy relations plus boundary conditions and from these derive the flow field. Here, a compatible flow field satisfying boundary conditions is taken as a starting point, validated by comparison to observed macrostructures, and from the flow field through equilibrium, constitutive, and energy relations weld torque and forces are determined. With the present approach, it is easier to ensure agreement between structure and dynamic effects. It is intended to use this approach to model defect formation in the future.

where the streamline enters the shear surface at radius, R , at angle θ_o . The omission of the $V/r\omega$ term in equation (11) assumes $V/r\omega \ll 1$, typically the case for FSW. The streamline approaching on the advancing side just grazes the shear surface at $\sin\theta_o = -1$ and the streamline follows the curve:

$$r \approx R - \frac{V}{\omega}(1 + \sin\theta). \quad (13)$$

As shown in figure 3, this corresponds to a circle of radius $R - V/\omega$ inside a shear surface of radius, R . The inner circle is displaced toward the advancing side by distance V/ω . This circle bounds a circular flow shown darkened in figure 3. The shear surface bulges out from the inner circle by distance $2V/\omega$ on the retreating side to accommodate the backflow of intercepted metal around the shear surface.

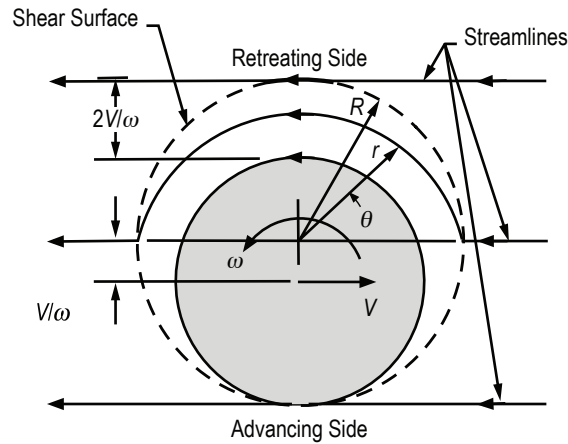


Figure 3. Streamlines in superposed rotating plug and uniform flow fields. Compare with figure 1. The advancing side streamline circumscribes a rotating eddy shown darkened. As there is no flow perpendicular to a streamline, no flow enters or leaves the eddy, which can be replaced by the friction stir pin.

Because the circle is a streamline, there is no flow perpendicular to the line and no metal flows in or out. Hence, the metal included in the circular flow is isolated. One can imagine scooping out all or some of the metal inside the circular flow and replacing it with the FSW pin without effect on the flow outside. This is where the FSW pin is located. At the end of the pin, the pin occupies the entire circular flow zone. Closer to the shoulder, where the shear surface flares out, the circular flow expands to incorporate the rotating plug metal as well as the pin. This is why in welding abrasive metal matrix composites, extensive pin wear begins at the end of the pin; closer to the shoulder, the pin is shielded by a layer of rotating plug metal.

Between the shear surface and the circular flow, weld metal flows in and out of the rotating plug. One can imagine trying to walk across a giant turntable. Before getting very far into the turntable, the table has rotated you to the opposite side and you are walking off the table.

By entering on the advancing side, you can get as far into the turntable as possible, skirting the forbidden circular flow area. Those crossing a rapidly rotating turntable remain close to its periphery; they do not get far in before they find themselves walking off the trailing edge. The flow around the FSW pin tends to be confined to a thin region at the periphery of the shear surface. This area is greatly exaggerated in figure 3.

What happens at the bottom of the pin? Given a lead angle, ϕ , there is a flow velocity component $V \sin \phi$ upward against the tool and out from under the pin. An encounter between this flow and a flow down the pin is often visible in FSW microstructures in a locale prone to wormhole formation.

If the shear surface descends all the way to the anvil, fine-grained nugget material can be seen on the root surface of the weld. If the shear surface does not descend to the anvil, a distorted but poorly bonded segment of weld metal may be left at the root of the weld, a 'lack of penetration' defect. How close the end of the pin has to be to the anvil for the shear surface to descend to the anvil is a matter of which is the easier mode of deformation.⁸

Lateral displacement is introduced by a third component flow, the ring vortex flow. Superposed rotating plug and uniform flow fields alone exhibit no lateral (or axial) displacement of streamlines.

2.4 Tool Geometry Effects: The Ring Vortex Flow Component Field

Threads on the pin, scrolls on the shoulder, tool orientation, or any feature of the FSW process inducing axial or radial flow may induce a ring vortex circulation all around the tool, like an encircling smoke ring. Flow down the pin induced by threads must eventually turn around in a circulation as it is trapped between anvil and shoulder. Heurtier et al. incorporated a ring vortex in a fluid-based FSW model in 2006.⁹ The concern here is not so much with the mathematical representation of the ring vortex as with its metallographic consequences.

The ring vortex flow passes through the shear surface. A radially inward component of the ring vortex flow field retains metal in the rotating plug so that it rotates farther before emerging into the tool wake. This causes a lateral displacement toward the advancing side of the tool. A radially outward component of the ring vortex flow field displaces metal off the rotating plug prematurely and shifts it toward the retreating side. If a radial velocity component, v , (positive outward) is superposed on equation (9),

$$\frac{dr}{dt} = v - V \cos \theta. \quad (14)$$

If the lateral distance is $y \approx R \sin \theta$, the net lateral displacement of a streamline entering the rotating plug at y_o away from the centerline path is

$$\left(\frac{y}{R} - \frac{y_o}{R} \right) \approx \frac{v}{V} (\theta - \theta_o). \quad (15)$$

With a ring vortex circulation, then, the FSW streamlines exhibit lateral displacements.

The streamlines along the weld seam are of considerable interest. They mark out the trace of the seam, shown schematically in figure 4. The welding action occurs on this line. If the pressure is insufficient to push down asperities or if contamination blocks adequate metal-to-metal contact a portion of the surface could remain unbonded. The term ‘kissing bond’ is sometimes applied to this situation. Given a weld with reduced strength, the seam trace is a region of suspicion, where defects may be found.¹⁰ In a sound weld, the seam trace is not easily discerned, but it is clearly revealed by tracers placed on the weld seam.^{11–14} ‘Residual oxide defect,’ where oxides on the faying surfaces prevent a sound bond,¹³ can greatly reduce the strength of a weld.

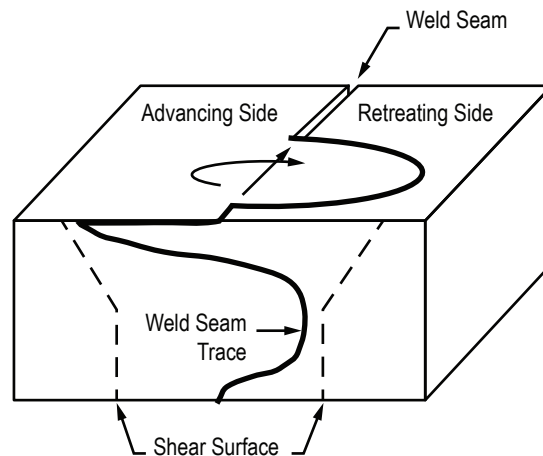


Figure 4. The trace of the weld seam takes a ‘lazy S’ shape (or sometimes a ‘zigzag’ shape) in a conventional friction stir weld due to the action of the ring vortex flow field component.

Why the ‘lazy S’ shape? The ring vortex flow close to the shoulder is inward in conventional welding practice. That is, v is negative in equation (14) and the streamlines are negatively displaced toward the advancing side. Farther away from the shoulder the ring vortex flow component becomes outward, and the seam trace is deflected to the retreating side of the weld. In 1999, Kevin Colligan used steel shot tracers to reveal the streamlines themselves in friction stir welds in 6061 and 7075 aluminum alloys.²

The lazy S contour is also seen bounding the joint between metals in bimetallic welds. A schematic division of flows in a simple bimetallic weld without a lateral displacement is shown in figure 5(a).

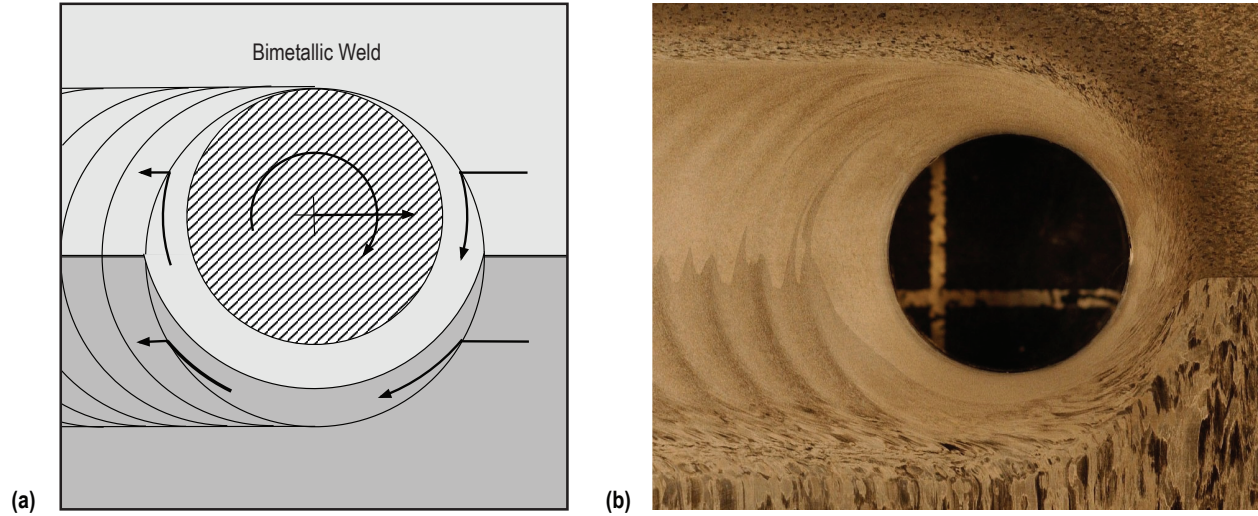


Figure 5. Plan views of bimetallic FSW weld: (a) Basic division of flows—metal on the retreating side flows over that on the advancing side. Alterations in contrast due to grain refinement are not shown. Complications arise due to the ring-vortex circulation (lateral displacement of the seam trace), oscillations (a wavy seam trace), or significant differences in flow stress (complex) and (b) 2219 aluminum alloy (advancing side) versus 2195 aluminum alloy (retreating side) (courtesy of G. Bjorkman, Lockheed Martin).

Figure 6 shows how the flow at the trailing edge of the shear surface may be in or out of the rotating plug. If an inward directed vortex component is not counteracted by an outward directed radial component of the uniform through-flow, $V\sqrt{1-\left(\frac{y}{R}\right)^2}$, the net flow of metal is into the rotating plug. The net outflow is determined in equation (16):

$$\frac{dr}{dt} \approx v + V\sqrt{1-\left(\frac{y}{R}\right)^2} . \quad (16)$$

The flow into the shear surface leaves deformed but recognizable parent metal in its wake, as seen on the weld transverse section. (The flow into the shear surface spirals axially down within the plug of metal rotating with the tool and emerges further down the pin where the net radial flow becomes outward.) The intrusions of parent metal into nugget material in the wake of a weld are called ‘flow arms.’ From equation (16), the condition for a flow arm is

$$\left(\frac{y}{R}\right)^2 > 1 - \left(\frac{v}{V}\right)^2 . \quad (17)$$

Flow arms appear near the shoulder where the ring vortex circulation radial component is negative and on the outer edges of the flow, where the radial outward component of the uniform through-flow is small.

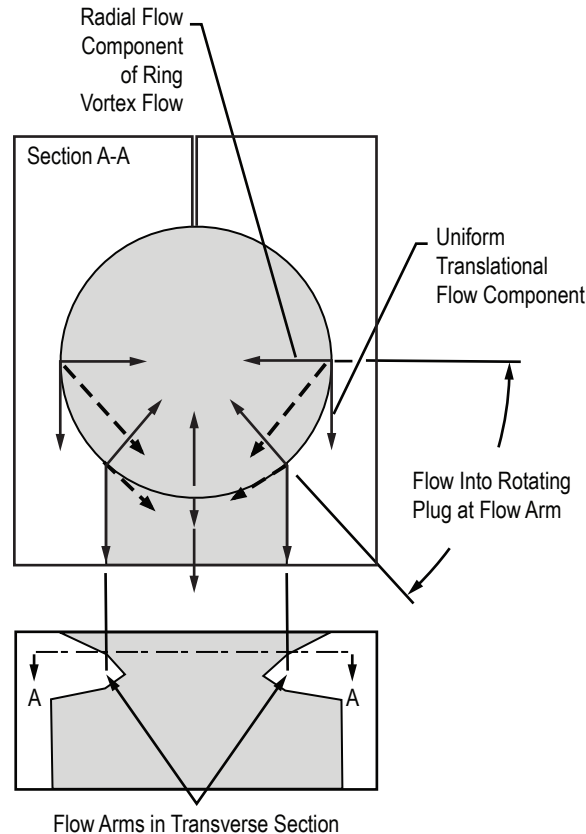


Figure 6. Flow arms, where the parent metal apparently penetrates into refined nugget material, are seen where the outward radial component of the translational flow is less than the inward radial component of the ring vortex circulation.

Flow arms are deeper when the ring vortex circulation is larger. If the inward radial velocity should equal or exceed the weld speed, the flow arms would meet according to equation (17) and a layer of parent metal would divide separate crown and root areas of nugget material. Higher levels of ring vortex circulation may be associated with hotter welds and reduced strength. Temperature and strength variations along a weld may be marked by flow arm variations. ‘Nugget collapse’ occurs in extreme conditions when the bulk of the recrystallized nugget material is displaced to the bottom of the weld.

Ring vortex streamlines trace paths from the weld metal surface under the shoulder down into the interior of the weld. The ring vortex circulation can entrain material from the crown surface of the weld metal into the interior.¹⁴

2.5 Tool Eccentricity Effects: Oscillations

Waves in streamlines close to the tool shoulder, textural banding in the interior of welds, and ripples on the weld surface in the wake of the weld or on the surfaces of internal cavities all testify to the presence of weld oscillations.

The oscillations synchronize with the tool rotation. They appear to be caused by tool eccentricity. If the tool is rigid and the weld metal is incompressible, the metal displaced by the tool must either be forced around the tool in a circumferential flow or out as ripples on the surface of the weld metal, or both. If the tool is not rigid, some of the eccentricity will be accommodated by tool deformation.

Assuming a rigid tool with pin radius, R , and eccentricity, ε , pushes the weld metal in and out as ripples at the weld metal surface, sinusoidal ripple contours with an amplitude as estimated below would be anticipated. Given a local radius, r , depending upon the tool eccentricity according to

$$r = R + \varepsilon \sin(\omega t + \varphi), \quad (18)$$

the ripple height, δ , can be estimated:

$$\delta = \varepsilon \frac{w}{R_s} \frac{R\omega}{V} \cos(\omega t + \varphi), \quad (19)$$

where

- w = the pin length
- R_s = shoulder radius
- ω = tool angular velocity
- V = weld speed
- φ = phase angle.

(Note that the ripple height remains the same from side to side of the weld because the reduced radial flow at the weld edges is compensated for by a reduced radial ripple spacing.)

Measurements of ripple height reported below^{15,16} are proportional to eccentricity, but the magnitudes are only a small fraction, in the present case, about 1.5%, of the estimate of equation (19). This implies that most of the eccentric displacements are either elastic or due to circumferential flow. Ripple contour shapes, as shown in figure 7, often differ from sinusoidal,¹⁵ especially under load control, where the shoulder can move up and down so as to vary the ripple emission rate.

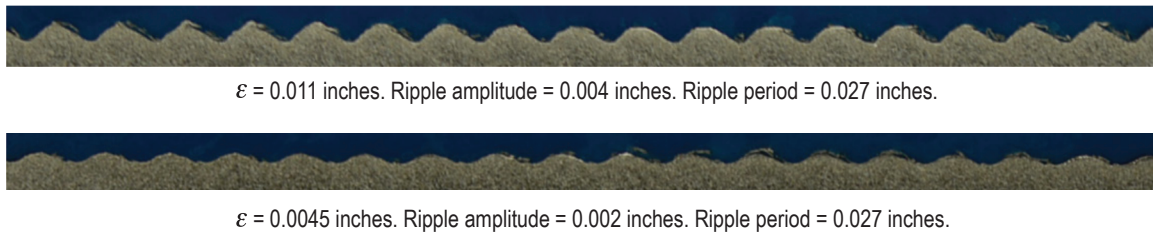


Figure 7. Ripple contours: $R = 0.250$ in, $R_s = 0.600$ in, $w = 0.315$ in, 220 RPM, 6 in/min, position control.¹⁶

Band contrast develops at the shear surface as shown in figure 8. Metal flows out along the shear surface to form the ripples. Variations in the outward (ripple) flow superposed upon the circumferential shearing flow produce textural variations. When polished and etched, the textural variations reflect light differently and appear as bands. The ring vortex circulation distorts the bands; it causes them to bulge out toward the bottom of the pin, where, in transverse section, they are seen as an ellipsoidal ‘onion ring’ pattern.

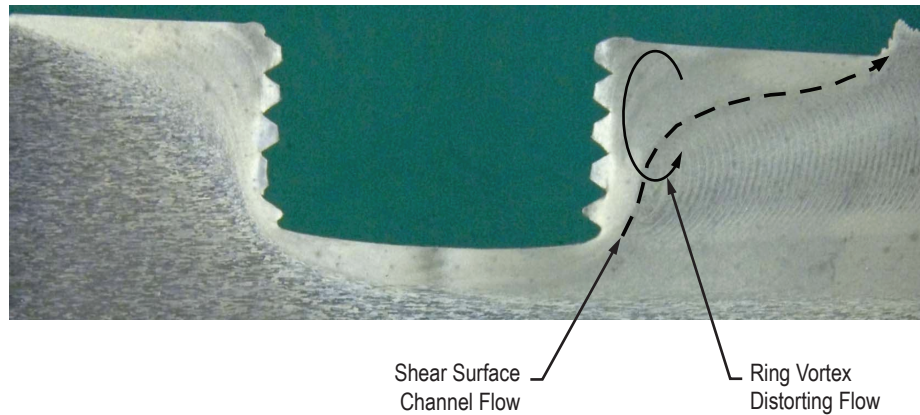


Figure 8. Longitudinal section of a partial penetration friction stir weld cavity in 2219 aluminum alloy (400 RPM, 2 in/min, 3° lead angle, 0.5–20 NF thread, courtesy of J.C. McClure). Internal bands and ripples can be seen emerging from the trailing edge of the shear surface. The bands are distorted in the ring vortex circulation.

Weld macrostructure may reveal considerable detail regarding the tool that made the weld. Tool modifications affect bands and ripples. Machining flats on the tool effectively reduces the ring vortex circulation (driven by the threads) and flattens the bulge seen in transverse section as the ‘onion ring’ pattern.⁴ The flats interrupt the periodic axial flow produced by tool eccentricity. This introduces additional sub-bands within the original eccentricity bands. With more than three flats, the interruptions coalesce into a new set of bands.

Close to the shoulder, streamline tracers show a lateral oscillation.² Similar lateral oscillations are seen in the boundary between metals joined in a bimetallic bond as shown in figure 5(b). Planar oscillations of tracers and of the seam trace can be produced by shear surface radius variations. If the radial velocity is much smaller than the weld speed, and if the shear surface radius, r , has a sinusoidal perturbation, $r = R - \Delta R \sin \theta$, then the lateral $y - y_0$ deflection of a tracer entering the shear surface may be estimated:

$$\frac{y - y_0}{R} \approx \left(\frac{\Delta R}{R} \right) \left(\frac{R\omega}{V} \right) \sin \theta . \quad (21)$$

In figure 5(b) the deflection appears to be around 8% of the shoulder radius and a somewhat larger percentage of the smaller shear surface radius at the location of the planar section. The parameters for the weld are not given, but the quantity $R\omega/V$ is, in general, large and a value of 20 or more would be reasonable to assume. Thus, a very small shear surface variation amplitude on the order of 0.4% of the shear surface radius would be sufficient to cause observable seam trace oscillation.

Ripples in the weld metal surface emanating from the edge of the shoulder caused by tool eccentricity presumably induce periodic pressure and friction variations at the edge of the shoulder, which are the likely cause of shear surface radius variations. In this model, the periodic variation of shear surface radius and the planar streamline oscillation amplitude are largest close to the shoulder and disappear by the center of the pin. Planar streamline oscillations close to the shoulder but not deeper into the weld have been observed with tracers.²

2.6 Summary: The Interpretation of Friction Stir Weld Structures

In table 1, a number of structural features observed on FSW sections are related to the flow components associated with them. For example, the shear surface is associated with the rotating plug flow component alone, while the lazy-S configuration of the seam trace is a result of the interaction of the rotating plug with the ring vortex flow components. Internal banding and surface ripples are a result of the interaction of the rotating plug flow component with oscillations, and so forth.

Table 1. Structural features related to flow components.

	Rotating Plug Component	Uniform Flow Component	Ring Vortex Flow Component	Oscillations
Rotating plug component	Shear surface	Nugget grain refinement; retreating side dispersion/bulge; tracer fractures	Lateral displacement of streamlines; lazy-S or zigzag curve of seam trace	Internal bands (onion ring pattern) and surface ripples
Uniform flow component	Nugget grain refinement.; retreating side dispersion/bulge; tracer fractures	–	Flow arms	–
Ring vortex flow component	Lateral displacement of streamlines; lazy-S or zigzag curve of seam trace	Flow arms	Axial and radial displacement of streamlines	–
Oscillations	Internal bands (onion ring pattern) and surface ripples	–	–	–

In figure 9(a), a schematic synthesis of features seen on a transverse weld section is shown as built up by incorporation of various FSW flow components. A transverse section of an actual friction stir bead-on-plate in 0.5-in-thick, 2219 aluminum alloy is shown in figure 9(b) for comparison.

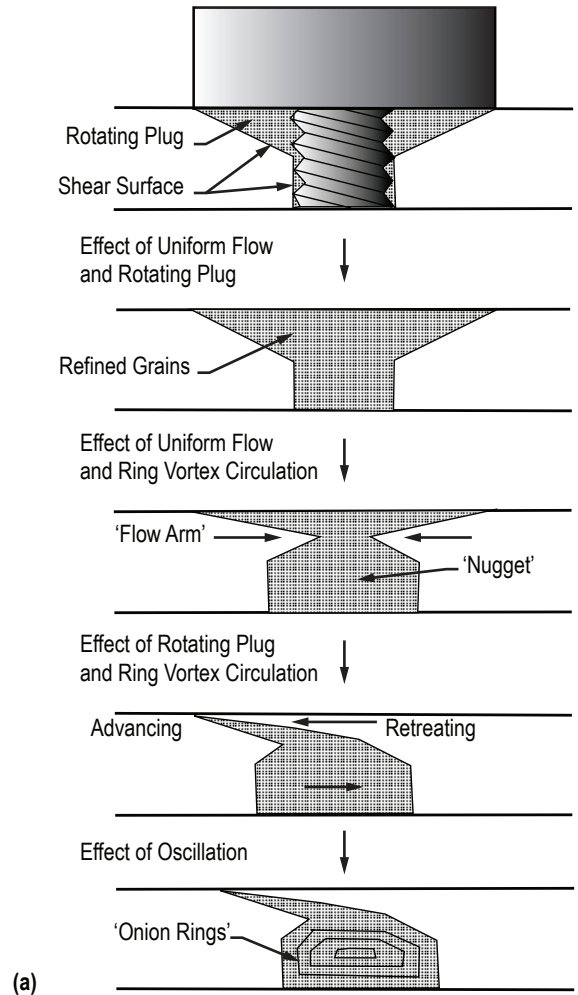


Figure 9. Transverse weld: (a) Schematic synthesis of features due to various FSW flow components on transverse weld section and (b) transverse bead-on-plate section in 0.5-in-thick, 2219 aluminum alloy (400 RPM, 2 in/min, 3° lead angle, courtesy of J.C. McClure).

In table 2 the flow components are related to controlling factors within weld parameters and tool geometry.

Table 2. Flow field components related to controlling factors.

Flow Field Component	Controlling Factors
Rotating plug	Tool rotation (RPM) Plunge force (to prevent slip at tool surface)
Uniform flow	Tool translation (weld speed)
Ring vortex	Tool surface threads, scrolling Tool lead angle
Oscillation	Tool eccentricity, flats

3. TEMPERATURES IN FRICTION STIR WELDING

The concept of the shear surface enables a simplified, approximate estimate of the temperature distribution in the vicinity of a friction stir weld. It leads to tentative computations of the torque, drag, and lateral forces for a FSW weld, which are compared to two empirical examples.

As discussed above, the main deformation zone around a rotating pin seized in metal contracts to a shear surface encapsulating the pin. This is because the flow stress of metals is so insensitive to strain rate that a very steep gradient in angular velocity is necessary to compensate for temperature effects that would otherwise raise the flow stress and prevent steady-state equilibrium. There is also a relatively slow extended deformation flow field around the FSW tool. For purposes of the temperature computation, the slow, extended field will be ignored.

The sole heat input will be taken as the mechanical power input at the shear surface. The sole heat loss, which balances the heat input under steady-state conditions, will be taken as conduction to the workpiece. Below this level of simplification, a number of parametric and geometric features affect the temperature. For example, heat losses to weld metal hold-down clamps can be inferred from noticeable torque variations correlating with tool positions relative to the hold-down clamps.¹⁷ Here, the potentially complex multiplicity of specifics is neglected, and a simplified approximation sought.

3.1 Temperature Variation Over the Shear Surface (Part 1)

Weld temperature is determined by a balance between power input and power loss. Wherever a mechanism produces power, under steady conditions that power must be removed. When that power is removed by heat conduction a thermal gradient is required. The more power generated at a site, the larger the temperature difference between that site and the environment. Given a fixed environmental temperature, the local site temperature rises and falls with the power generated at that site.

In order to determine the temperature variation within the workpiece it is necessary to know how the power input at each site in the workpiece varies and the relation between the power to be dissipated and the local temperature. This could be a very complex problem due to the geometry alone if handled in its full generality even if the properties of the workpiece material were fully known. But the flow stress of the weld metal is a function of thermomechanical history, and this function is not well known. Thermal conductivity is also a poorly known function of thermomechanical history.

But, this potential complexity shall not be intimidating. The computation of temperatures on the shear surface shall be made tractable, and even simple by the use of approximations that capture enough of the reality of the situation to deliver useful results for interpreting the observed relations of temperatures, torques and forces to weld parameters, and tool geometries. The simplifying assumptions invoked to make the computation tractable are as follows.

First, the entire power input is taken to be generated at the shear surface where the shearing rate is large. The power generated in the extended auxiliary flow, where the shearing rate is relatively small, is ignored. As discussed above, the weld metal is taken to be sticking to the tool surface; in the absence of shear at the sticking surface, no power is generated there. The heat carried by the uniform flow of metal is added to or subtracted from that generated at the shear surface.

Second, the weld metal flow stress at the shear surface, where heat is generated, is approximated as a linear function of temperature descending to zero at the melting temperature. This approximation holds only if temperatures at the shear surface remain above approximately 75% of the melting temperature.

Third, circumferential and axial heat flow is ignored. All the heat generated at the shear surface is taken to exit radially. This allows the heat flow environment of the friction stir tool to be sliced into sectors, each sector associated with an element of the shear surface area as shown in figure 10. The temperature of each element is uniquely determined by a heat flow balance between the heat generated at the element and the heat conducted away through the environmental sector. The heat is conducted away to a fixed distance where the temperature is effectively the ambient temperature of the workpiece. The ambient temperature is here taken to be a constant, but for a small, insulated workpiece, the ambient temperature could be taken to rise as the workpiece heats up.

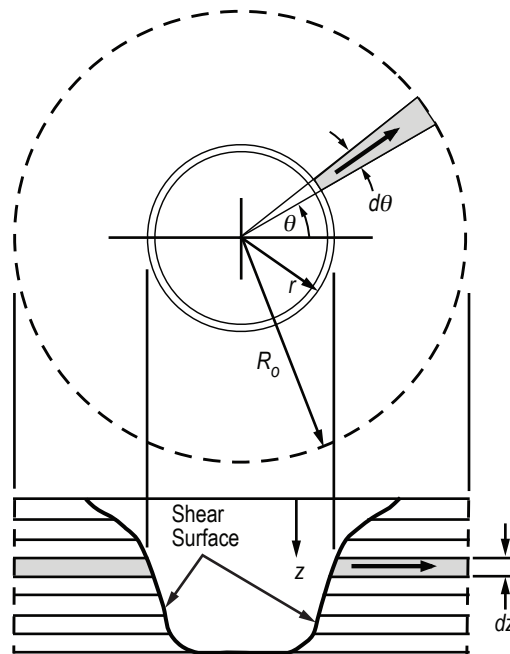


Figure 10. Subdivision of the volume outside the FSW shear surface into slices of thickness, dz , and the slices into sectors of angle, $d\theta$. Heat is taken to flow from the shear surface through each sector independently to radius, R_o , at ambient temperature, T_o .

Note that the thermal conductivity is taken simply as the room temperature value. Annealing could raise the conductivity (by about 30% in the case of 2219 aluminum), but annealing takes time and the FSW thermomechanical history of a weld metal element is presumably too rapid for a full anneal although significant solution and precipitation effects apparently occur.¹⁸ The thermal conductivity of metals is due mainly to the free electrons. The electrons carry more heat as the temperature rises. For pure aluminum above room temperature the electrical conductivity decreases and the thermal conductivity remains roughly the same.¹⁹

Given the thermal conductivity of an aluminum alloy such as 2219 aluminum is on the order of 5 times that of a typical tool steel at anticipated processing temperatures, for our rough approximation, tool heat losses are neglected and all heat losses are assumed to the workpiece. Further, the workpiece shall be subdivided into slices of thickness, dz , and the slices subdivided into sectors of angle, $d\theta$, as shown in figure 10. Differences in temperature emerge at the shear surface, as required, to conduct heat away at different rates from the shear surface.

For a steady radial heat flow rate, dQ_{cond} , conducted down a sector:

$$dQ_{\text{cond}} = \frac{k}{\ln \frac{R_o}{r}} (T - T_o) d\theta dz, \quad (22)$$

where

- k = thermal conductivity of the weld metal
- T = shear surface temperature at radius, r
- T_o = ambient temperature at radius, R_o .

The logarithm term in equation (22) is not very sensitive to R_o/r , which can be approximated by a constant. As the temperature around an FSW pin tool drops off so rapidly that temperatures close to ambient are attained within 5 or 10 pin radii from the tool, anticipated values for the constant would be around 5 or 10.

The power generated at the shear surface, dQ_{gen} is

$$dQ_{\text{gen}} = \tau r d\theta \sqrt{dr^2 + dz^2} (r\omega - V \sin \theta), \quad (23)$$

where τ = flow stress and ω = angular velocity of the shear surface.

3.2 Flow Stress Dependence on Strain Rate and Temperature

Supposing that the flow stress acts to reduce the thermal activation energy, E , needed for dislocations to pass through pinning barriers, an approximate relation between strain rate, flow stress, and temperature can be written:

$$\dot{\gamma} = \dot{\gamma}_o e^{-\frac{E-\tau v}{\kappa T}} \quad (24)$$

or

$$\tau = \frac{E}{v} - \left(\frac{\kappa}{v} \ln \frac{\dot{\gamma}_o}{\dot{\gamma}} \right) T, \quad (25)$$

where

- $\dot{\gamma}$ = actual strain rate
- $\dot{\gamma}_o$ = maximum unhindered strain rate
- v = 'activation volume,' a constant approximating the effect of stress upon the activation energy, E
- κ = Boltzmann's constant.

Anticipating $\dot{\gamma}_o / \dot{\gamma}$ to be large and its logarithm roughly constant, equation (25) suggests a linear dropoff of flow stress with temperature with negligible dependence upon strain rate. Measurements of flow stress for a wide range of strain rates shows only a weak dependence on strain rate.⁶ Neglecting strain rate dependence, and taking the flow stress as zero at the (solidus) melting temperature, T_{melt} , a simple approximation to the flow stress close to melting where the FSW shear surface temperatures are anticipated to lie can be constructed:

$$\tau = \left(-\frac{\partial \tau}{\partial T} \right) (T_{\text{melt}} - T). \quad (26)$$

$(-\partial \tau / \partial T)$ is a constant, theoretically equal to $\kappa / v \ln \dot{\gamma}_o / \dot{\gamma}$ according to equation (25), but this constant is difficult to estimate. An empirical estimate can be obtained from strength data²⁰ taken close to the melting point and recalling from maximum shear theory that the flow stress in shear is about half that in tension. See figure 11 representing the variation of flow stress with temperature for 2219-T81 aluminum alloy. As the temperature falls, structural obstacles to phonon motion become more stable, the flow stress rises, and structure sensitivity rises so that below the neighborhood of half the melting temperature, wide variations in strength, depending upon temper condition, are seen. Close to the FSW tool, where the bulk of the FSW flow takes place, typical temperatures tend to be in the range where equation (26) represents the flow stress temperature dependence reasonably well.

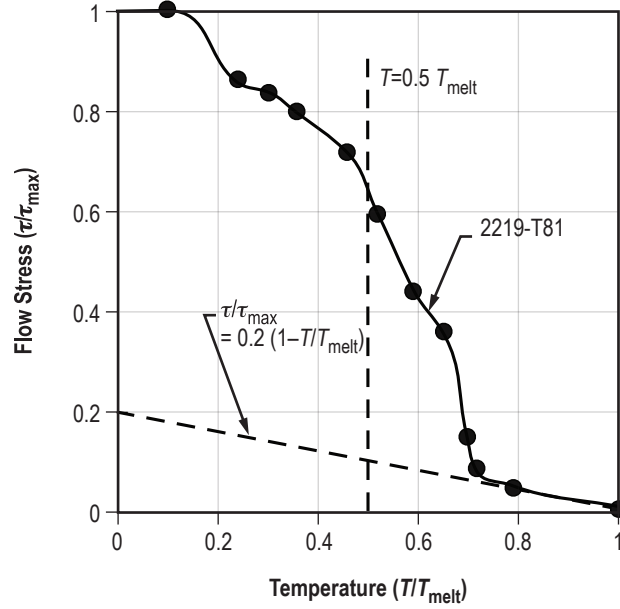


Figure 11. Estimate of flow stress temperature dependence from typical ultimate tensile strength versus temperature data in ASM Metals Handbook.²⁰ Flow stress is assumed proportional to the ultimate tensile strength. The linear

approximation $\tau = \left(-\frac{\partial\tau}{\partial T}\right)(T_{\text{melt}} - T)$, where $\left(-\frac{\partial\tau}{\partial T}\right) \approx \frac{0.2\tau_{\text{max}}}{T_{\text{melt}}} \sim 5.9 \frac{\text{psi}}{^{\circ}\text{K}}$, holds down to around $0.75 T_{\text{melt}} \approx 340^{\circ}\text{C}$ and encompasses the anticipated range of FSW temperatures.

3.3 Temperature Variation Over the Shear Surface (Part 2)

The motion of the tool through the weld metal introduces a convective heat loss. As the FSW tool moves into cooler ambient temperature metal, it loses energy to heat the metal to the temperature of the shear surface. The convective loss, dQ_{conv} , is approximated:

$$dQ_{\text{conv}} = \rho C (T - T_o) V r \cos \theta d\theta dz, \quad (27)$$

where

ρ = the weld metal density

C = specific heat

V = the weld speed.

The heat is lost at the leading edge of the shear surface where the cold metal enters the shear surface. At the trailing edge, however, the heat lost is regained as an additive contribution to the heat that must be rejected through the sectors on this surface. The $\cos \theta$ term accounts for both effects; it is positive on the leading edge and negative on the trailing edge.

The heat balance for estimation of the temperature at a point on the shear surface based on the above approximations is

$$dQ_{\text{gen}} = dQ_{\text{cond}} + dQ_{\text{conv}} \quad (28)$$

or

$$\begin{aligned} & \left[\left(-\frac{\partial \tau}{\partial T} \right) (T_{\text{melt}} - T) \right] r (r\omega - V \sin \theta) \sqrt{1 + \left(\frac{dr}{dz} \right)^2} d\theta dz \\ & = \frac{k}{\ln \frac{R_o}{r}} (T - T_o) d\theta dz + \rho C (T - T_o) V r \cos \theta d\theta dz. \end{aligned} \quad (29)$$

Solved for the temperature, this becomes

$$\begin{aligned} (T - T_o) = & \frac{1}{\frac{1}{\ln \frac{R_o}{r}} \frac{k}{r^2 \omega \rho C} + \frac{V}{r\omega} \cos \theta} (T_{\text{melt}} - T_o) \cdot \\ & 1 + \frac{\frac{1}{\rho C} \left(-\frac{\partial \tau}{\partial T} \right) \sqrt{1 + \left(\frac{dr}{dz} \right)^2} \left(1 - \frac{V}{r\omega} \sin \theta \right)}{r} \end{aligned} \quad (30)$$

From equation (30), it is apparent that as the angular velocity increases, the temperature of the shear surface approaches the melting temperature of the weld metal. As the thermal conductivity of the weld metal and the weld speed increase, the shear surface temperature drops. Increasing the shear surface radius and inclining its slope raises its temperature.

There are two sources of circumferential temperature variation:

(1) There is a side-to-side ($\sin \theta$) variation caused by differences in shear rate along the shear surface. While the shear surface moves forward at velocity, V , the circumferential velocity of the circumference is not quite $r\omega$, but actually $r\omega - V \sin \theta = r\omega (1 - V/r\omega \sin \theta)$. If the shear rate perturbation is small, so is the shear stress perturbation. The revised power dissipation per unit area amounts to approximately $\tau r\omega (1 - V/r\omega \sin \theta)$. Local conduction losses as approximated by equation (22) are proportional to the difference between the local temperature and ambient temperature. If the mean surface temperature difference $(\bar{T} - T_o)$ is sufficient to dissipate the mean power, then to dissipate the perturbation power, a temperature perturbation of approximately $-(\bar{T} - T_o) V / r\omega \sin \theta$ would be required. This is identical to the approximate relation in equation (32) derived from equation (30), assuming small values of $V/r\omega$.

(2) There is also a back-to-front ($\cos \theta$) variation caused by the encounter with cooler, ambient temperature metal at the leading edge of the shear surface. The local temperature perturbation is proportional to the extra power per unit area, approximately $\rho C(\bar{T} - T_o)V \cos \theta$, fed in (or extracted at the leading edge) by metal moving into the shear surface compared to the overall power loss by conduction, $\tau r \omega = r \omega \left(-\frac{\partial \tau}{\partial T} \right) (T_{\text{melt}} - T_o)$. That is,

$$\begin{aligned}
 (T - T_o)_{\text{conv}} &\approx \frac{\rho C(\bar{T} - T_o)V \cos \theta}{r \omega \sqrt{1 + \left(\frac{dr}{dz} \right)^2} \left(-\frac{\partial \tau}{\partial T} \right) (T_{\text{melt}} - T_o)} (\bar{T} - T_o) \\
 &\approx \left[\frac{(\bar{T} - T_o)}{\frac{1}{\rho C} \left(-\frac{\partial \tau}{\partial T} \right) \sqrt{1 + \left(\frac{dr}{dz} \right)^2} (T_{\text{melt}} - T_o)} \frac{V}{r \omega} \cos \theta \right] (\bar{T} - T_o) \\
 &\approx \left[\frac{\frac{V}{r \omega}}{\frac{1}{\rho C} \left(-\frac{\partial \tau}{\partial T} \right) \sqrt{1 + \left(\frac{dr}{dz} \right)^2} + \frac{1}{\ln \frac{R_o}{r}} \frac{k}{r^2 \omega \rho C}} \cos \theta \right] (\bar{T} - T_o).
 \end{aligned} \tag{31}$$

Again, this is the same as in equation (32).

$$(T - T_o) \approx (\bar{T} - T_o) \left[1 - \frac{V}{r \omega} \sin \theta - \frac{\frac{V}{r \omega} \cos \theta}{\frac{1}{\rho C} \left(-\frac{\partial \tau}{\partial T} \right) \sqrt{1 + \left(\frac{dr}{dz} \right)^2} + \frac{1}{\ln \frac{R_o}{r}} \frac{k}{r^2 \omega \rho C}} \right], \tag{32}$$

where

$$(T - T_o) \approx (\bar{T} - T_o) \left[1 - \frac{V}{r\omega} \sin\theta - \frac{\rho C (\bar{T} - T_o) V \cos\theta}{r\omega \left(-\frac{\partial\tau}{\partial T} \right) (T_{\text{melt}} - T_o) \sqrt{1 + \left(\frac{dr}{dz} \right)^2}} \right]. \quad (33)$$

4. TORQUES AND FORCES IN FRICTION STIR WELDING

The shear surface separates the tool (and an attached rotating plug of metal) from the weld metal. At each element of the shear surface the surrounding metal exerts a local shear stress τ and a local pressure P . A local shear force and pressure force are determined by multiplying the shear stress and pressure times the local area upon which they act as shown schematically in plan section in figure 12.

The local shear forces act at the end of a radius from the tool center of rotation so as to produce a moment about the tool center of rotation. The total moment exerted on the tool then constitutes a summation or integral over the total shear surface of the local moments as described in equation (34). In order to evaluate the integral it is necessary to know the value of the local shear stress distribution over the shear surface.

Both local shear and pressure forces have force components in the $-x$ or drag direction. By integrating the local drag components, as in equation (38), it is possible to estimate the drag force on the tool. In this case it is necessary to know the distribution of both shear and pressure forces over the tool surface. The lateral force can be estimated similarly from the components in the y direction, as in equation (39). Note that the integrals of shear and pressure components that do not vary with angular position θ vanish and do not contribute to the drag and lateral force. It is the variation of the local shear and pressure forces over θ that produces the tool forces.

The circumferential variation in shear stress may be obtained through equation (26) from the circumferential temperature variation estimated above in equation (30). The pressure is another matter. As the leading edge of the shear surface moves forward, the primary direction of motion of the metal incorporated into the rotating plug changes from radially into the plug to circumferential, a directional change of 90° . The pressure needed to affect this directional change is approximately $\pi\tau$, estimated through the slip-line theory of plasticity in analogy to the well-known estimate of the pressure required to indent a plastic surface, approximately $2\pi\tau$. This pressure component, which is proportional to the shear stress and hence varies circumferentially also, affects the drag and lateral force through equations (38) and (39), respectively. There is also a pressure component due to the plunge force acting on the tool; this pressure is assumed to be evenly distributed over the tool circumference so as not to contribute any drag or lateral force.

In order to estimate tool forces, the shape of the shear surface upon which the shear stress and pressure act is required. This could be approximated by the tool-weld metal interface, but, assuming that the weld metal sticks to the tool and shears within the bulk of the surrounding metal, a better approximation would be a flared cylinder as shown in figure 2, extending between the tool radius at the pin end and the shoulder radius at the weld surface. A semi-empirical shape, equation (43) is used for the present computations. A still better approximation would be arrived at from minimizing torque through calculus of variation techniques, but the added complications were considered not to be worth the small increment of precision. A flat surface is taken to close

the shear surface at the end of the pin. The effect of shear stress on this surface (pressure on this surface produces only axial forces) is accounted for in torque estimates, but is taken to cancel out and is ignored for drag and lateral force estimates.

4.1 Torque

The torque, M , required to turn the FSW tool is

$$M \approx \underbrace{\iint}_{\text{Lateral Shear Surface}} \tau r^2 \sqrt{1 + \left(\frac{dr}{dz}\right)^2} d\theta dz + \underbrace{\int}_{\text{Bottom Shear Surface}} \tau(z=0) r^2 d\theta dr. \quad (34)$$

The expression for the shear flow stress, equation (35), is simplified in approximation equation (36). This can be inserted into the moment expression, equation (34), to evaluate it in expression (37):

$$\tau = \left(-\frac{\partial \tau}{\partial T}\right)(T_{\text{melt}} - T) = \left[\frac{\frac{\frac{1}{\ln \frac{R_o}{r}} \frac{k}{r^2 \omega \rho C} + \frac{V}{r\omega} \cos \theta}{\frac{1}{\rho C} \left(-\frac{\partial \tau}{\partial T}\right) \sqrt{1 + \left(\frac{dr}{dz}\right)^2} \left(1 - \frac{V}{r\omega} \sin \theta\right)}}{\frac{\frac{1}{\ln \frac{R_o}{r}} \frac{k}{r^2 \omega \rho C} + \frac{V}{r\omega} \cos \theta}{1 + \frac{\frac{1}{\rho C} \left(-\frac{\partial \tau}{\partial T}\right) \sqrt{1 + \left(\frac{dr}{dz}\right)^2} \left(1 - \frac{V}{r\omega} \sin \theta\right)}}} \right] \left(-\frac{\partial \tau}{\partial T}\right)(T_{\text{melt}} - T_o) \quad (35)$$

$$\approx \frac{\frac{1}{\ln \frac{R_o}{r}} \frac{k}{r^2 \omega} (T_{\text{melt}} - T_o)}{\sqrt{1 + \left(\frac{dr}{dz}\right)^2}} + \frac{\frac{1}{\ln \frac{R_o}{r}} \frac{k}{r^2 \omega} \frac{V}{r\omega} (T_{\text{melt}} - T_o)}{\sqrt{1 + \left(\frac{dr}{dz}\right)^2}} \sin \theta + \frac{\frac{V}{r\omega} \rho C (T_{\text{melt}} - T_o)}{\sqrt{1 + \left(\frac{dr}{dz}\right)^2}} \cos \theta. \quad (36)$$

Inserting equation (36) into equation (34),

$$M \approx 2\pi \left(\frac{k}{\rho C} \right) \rho C (T_{\text{melt}} - T_o) \left[\int_0^w \frac{dz}{\ln \frac{R_o}{r}} + \frac{R}{\ln \frac{R_o}{r}} \right]. \quad (37)$$

Note that the torque is inversely proportional to the angular velocity, so that as long as the geometry does not change, the power, $M\omega$, is constant. It was observed early in investigations of FSW that the power is approximately constant.

4.2 Steady Tool Forces (Part 1)

In order to estimate the forces, it is necessary to estimate the pressure, P , at the shear surface:

$$F_{-x} = \int_{\text{Shear Surface}} \left[P \cos \theta - \tau \sqrt{1 + \left(\frac{dr}{dz} \right)^2} \sin \theta \right] r d\theta dz \quad (38)$$

and

$$F_{-y} = \int_{\text{Shear Surface}} \left[P \sin \theta + \tau \sqrt{1 + \left(\frac{dr}{dz} \right)^2} \cos \theta \right] r d\theta dz. \quad (39)$$

The tool forces are given in figure 12.

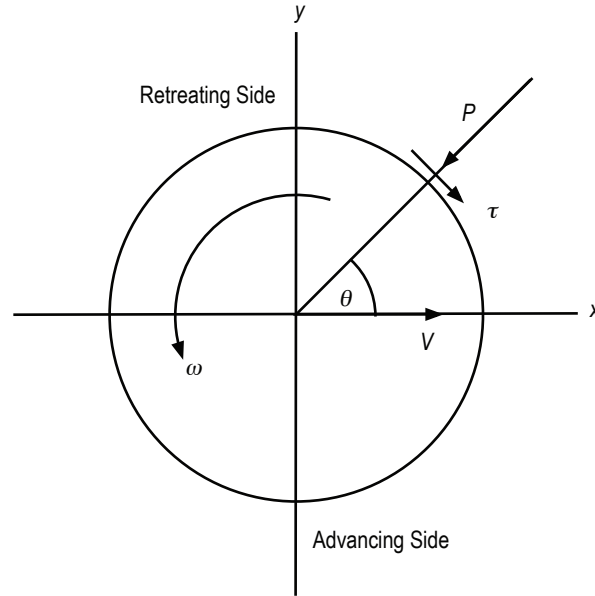


Figure 12. Local pressure, P , and shear, τ , on shear surface determine the tool forces.

4.3 Pressure Variation on Shear Surface

First, the static pressure is estimated using a hydrostatic model. Near the shear surface a relatively slow distributed quasi-viscous deformation is observed. The weld seam takes on a substantial curve before disappearing at the shear surface. The rotating plug of metal between the shear surface and the weld tool exhibits surface ripples extruded at the edge of the shoulder as well as associated banding throughout the interior of the weld. This suggests that the static pressure, P_{stat} , within the rotating plug may be approximated by a hydrostatic model, $P_{\text{stat}} \approx F_z / \pi R_s^2$. The static pressure is radially symmetrical and, in accordance with equations (38) and (39), does not contribute to the drag or lateral force.

If the tool is moved, the advancing edge of the shear surface compresses the metal ahead of it and the retreating surface extends the metal behind it. This results in a dynamic contribution to the pressure. If the metal were not to deform, the dynamic pressure would rise without limit; however, at some point, the metal gives way and limits the dynamic pressure. Because of the local constraints on deformation, the limiting pressure magnitude is greater than the approximately 2τ for a tensile test.

The local dynamic pressure, P_{dyn} , is determined by the excess pressure beyond the symmetrical hydrostatic pressure at which the radial incoming flow can ‘turn the corner’ to merge with the circumferential flow induced by the rotating tool. This requires rotating the streamline by 90° .

Moment equilibrium for a segment of weld metal shown schematically in figure 13, rotating into the circumferential flow at the shear surface, requires $P_{\text{dyn}} \cdot \delta \cdot \delta / 2 \approx \tau \cdot \pi \delta / 2 \cdot \delta$ or $P_{\text{dyn}} \approx \pi \tau$, where τ is the local weld metal flow stress. A similar result is obtained from slip-line theory. Hence, the pressure, P , at the shear surface is estimated at approximately

$$P \approx \frac{F_z}{\pi R_s^2} + \pi \tau(r, \theta, z). \quad (40)$$

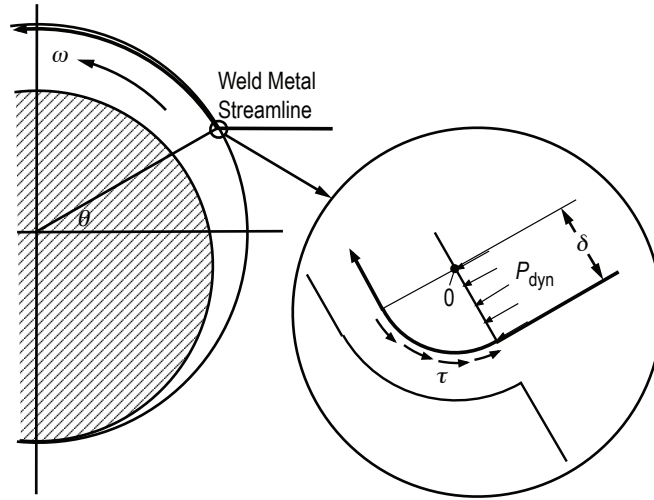


Figure 13. Weld metal entry into the circumferential flow around the tool is held back until the dynamic pressure, P_{dyn} , is large enough to overcome the local shear stress resistance to turning from radial to circumferential flow.

4.4 Steady Tool Forces (Part 2)

Combining equations (36), (38), and (40) results in

$$F_{-x} = \pi \rho C (T_{\text{melt}} - T_o) \frac{V}{\omega} \int_{\text{Shear Surface}} \left[\frac{\pi}{\sqrt{1 + \left(\frac{dr}{dz}\right)^2}} - \frac{1}{\ln \frac{R_o}{r}} \frac{k}{r^2 \omega} \right] dz. \quad (41)$$

Combining equations (36), (39), and (40) results in:

$$F_{-y} \approx \pi \rho C (T_{\text{melt}} - T_o) \frac{V}{\omega} \int_{\text{Shear Surface}} \left[\frac{\pi}{\sqrt{1 + \left(\frac{dr}{dz}\right)^2}} \frac{1}{\ln \frac{R_o}{r}} \frac{\frac{k}{\rho C}}{r^2 \omega} + 1 \right] dz . \quad (42)$$

Drag and lateral forces are comprised of two parts, a conduction and a convection component. (The conduction term contains the thermal conductivity, k .) The thermal diffusivity is $k/\rho C$, about $0.530 \text{ cm}^2/\text{s}$ for 2219-T87 aluminum alloy. For a 0.25-inch pin radius with a rotational speed of 150 RPM, $(k/\rho C)/R^2\omega \approx 0.0837$. If $R_s \approx 3R$ and $R_o \approx 6R$, then $0.558 \leq 1/\ln R_o/r$. This implies that the conduction term tends to be smaller than the convection term, which dominates ≤ 1.4 .

The conduction drag component is negative. The shear stress at the cooler retreating side of the tool is larger and tends to propel the tool through the workpiece in the same way that an automobile tire with its higher shear stress at the retreating/road side propels the automobile. In general, the convection term easily overcomes the conduction term; however, the convection term is reduced by a flatter shear surface profile, i.e., higher dr/dz . This suggests that a conical tool might reduce drag and that there could be shear surface regions near the outer edge of the shoulder that contribute negative drag.

In order to evaluate the integrals of equations (37), (42), and (43) and compute the torque, drag force, and lateral force, it is necessary to incorporate the shape of the shear surface, $r(z)$.

4.5 The Shape of the Shear Surface

Figure 14 illustrates a simplified shear surface. The sides comprise a flared cylinder. The bottom is flat.

The surface shape with minimal torque (the weak link) will presumably be the first to shear and will prevent the occurrence of any shapes requiring greater torque values. If the shape of the shear surface is represented by the approximation

$$r - R \approx \left(\frac{z}{w}\right)^n (R_s - R) \quad (43)$$

and

$$\frac{dr}{dz} \approx \frac{n}{w} \left(\frac{z}{w}\right)^{n-1} (R_s - R) . \quad (44)$$

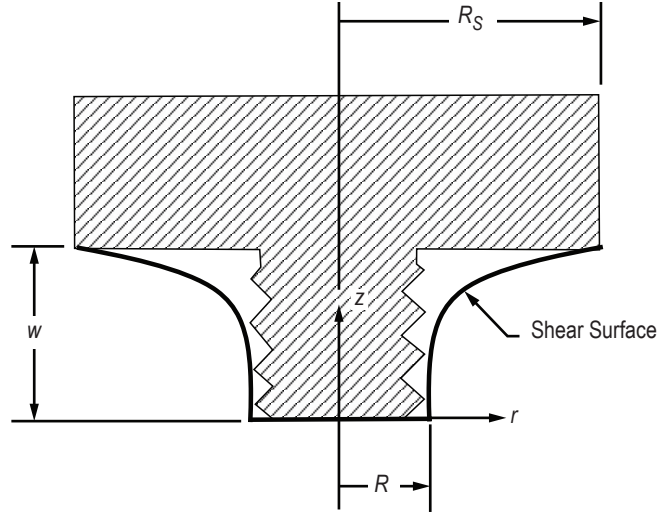


Figure 14. Simplified flared cylindrical shear surface with radius, $r(z)$ and flat bottom.

4.6 Torque, Drag, and Lateral Forces

From equations (37), (41), and (42),

$$M \approx \left[2\pi R^2 w \rho C (T_{\text{melt}} - T_o) \right] \frac{\left(\frac{k}{\rho C} \right)}{R^2 \omega} \left[\int_0^1 \frac{d\zeta}{\ln \frac{R_o}{R + \zeta^n \left(\frac{R_s}{R} - 1 \right)}} + \frac{\frac{R}{w}}{\ln \frac{R_o}{R}} \right], \quad (45)$$

$$F_{-x} = \frac{\pi}{2} \left[2Rw\rho C (T_{\text{melt}} - T_o) \right] \frac{V}{R\omega}.$$

$$\int_0^1 \left[\frac{\pi}{\sqrt{1 + \left[n \frac{R}{w} \zeta^{n-1} \left(\frac{R_s}{R} - 1 \right) \right]^2}} - \frac{1}{\left[1 + \zeta^n \left(\frac{R_s}{R} - 1 \right) \right]^2 \ln \frac{R_o}{R + \zeta^n (R_s - R)}} \right] \frac{\frac{k}{\rho C}}{R^2 \omega} d\zeta, \quad (46)$$

$$F_{-y} \approx \frac{\pi}{2} [2Rw\rho C(T_{\text{melt}} - T_o)] \frac{V}{R\omega}.$$

$$\int_0^1 \left[\frac{\pi}{\left[1 + \zeta^n \left(\frac{R_s}{R} - 1\right)\right]^2 \ln \frac{\frac{R_o}{R}}{1 + \zeta^n \left(\frac{R_s}{R} - 1\right)} \sqrt{1 + \left(\frac{n}{w} \zeta^{n-1} (R_s - R)\right)^2}} \frac{k}{R^2 \omega} + 1 \right] d\zeta. \quad (47)$$

4.7 Sample Computations: Torque, Drag, and Lateral Force

4.7.1 Example 1

For a pin radius, $R=0.250$ in and length $w=0.323$ in, a shoulder radius, $R_s=0.600$ in, estimating $R_o/R \approx 5$, and for 2195-T87 weld metal, it is possible to evaluate equations (45), (46), and (47).

For 2219-T87 aluminum alloy, $\rho C (T_{\text{melt}} - T_o)$ has the dimensions of a stress, about 185,100 psi, and $k/\rho C$ is a thermal diffusivity, about $0.530 \text{ cm}^2/\text{s}$.

The cross-sectional area of the tool, $2Rw=0.1615 \text{ in}^2$ when multiplied by the characteristic stress, $\rho C (T_{\text{melt}} - T) \approx 185,100$ psi, yields a force of 29,894 lb. The pin surface area times its radius, $2\pi R^2 w = 0.1268 \text{ in}^3$, when multiplied by the characteristic stress, yields a torque of 23,470 in-lb.

The angular velocity in radians per minute is $\omega = 2\pi \cdot \text{RPM}$. If weld speed, V , is measured in inches per minute, then

$$\frac{V}{R\omega} = \frac{V}{2\pi R \cdot \text{RPM}} \approx 0.6366 \frac{V}{\text{RPM}} \quad (48)$$

is a dimensionless number. Similarly dimensionless is

$$\frac{\frac{k}{\rho C}}{R^2 \omega} = \frac{\frac{k}{\rho C}}{2\pi R^2 \text{RPM}} = \frac{\left[0.530 \frac{\text{cm}^2}{\text{s}}\right] \left[\frac{1 \text{ in}}{2.54 \text{ cm}}\right]^2 \left[\frac{60 \text{ s}}{\text{min}}\right]}{2\pi [0.250 \text{ in}]^2 \left[\text{RPM} \frac{1}{\text{min}}\right]} = \frac{12.55}{\text{RPM}}. \quad (49)$$

The moment, M , would be minimized by a very large value for n , but observations suggest values of 2 or 4 would more realistically describe the shape of the shear surface. If a value of $n=4$ is taken, the resulting moment and force computations become

$$M \approx \left[\frac{294,500}{\text{RPM}} \text{ in-lb} \right] \left[\int_0^1 \frac{d\zeta}{\ln \frac{5}{1+1.4\zeta^4}} + \frac{0.774}{\ln 5} \right] \approx \frac{361,793}{\text{RPM}} \text{ in-lb} , \quad (50)$$

$$F_{-x} \approx [29,893 \text{ lb}] \frac{V}{\text{RPM}} \int_0^1 \left[\frac{\pi}{\sqrt{1+18.78\zeta^6}} - \frac{1}{(1+1.4\zeta^4)^2 \ln \frac{5}{1+1.4\zeta^4}} \frac{12.55}{\text{rpm}} \right] d\zeta$$

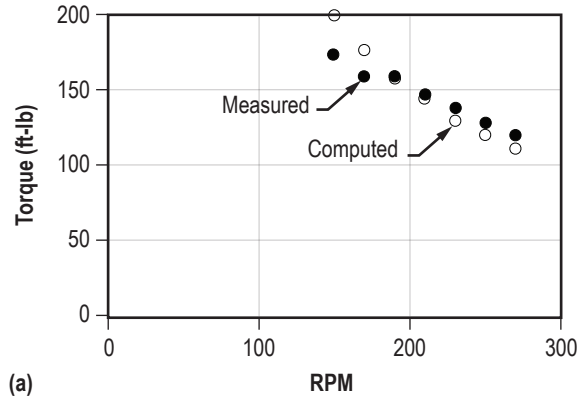
$$\approx 70,009 \frac{V}{\text{RPM}} \left(1 - \frac{2.671}{\text{RPM}} \right) \text{ lb} , \quad (51)$$

and

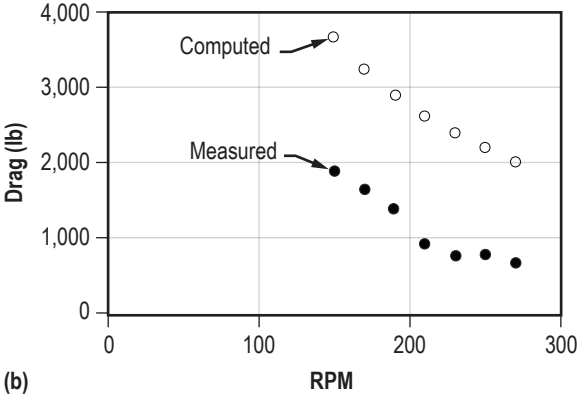
$$F_{-y} \approx [29,893 \text{ lb}] \frac{V}{\text{RPM}} \int_0^1 \left[\frac{\pi}{(1+1.4\zeta^4)^2 \ln \frac{5}{1+1.4\zeta^4} \sqrt{1+18.78\zeta^6}} \frac{12.55}{\text{RPM}} + 1 \right] d\zeta$$

$$\approx 29,893 \frac{V}{\text{RPM}} \left(1 + \frac{19.65}{\text{RPM}} \right) \text{ lb} . \quad (52)$$

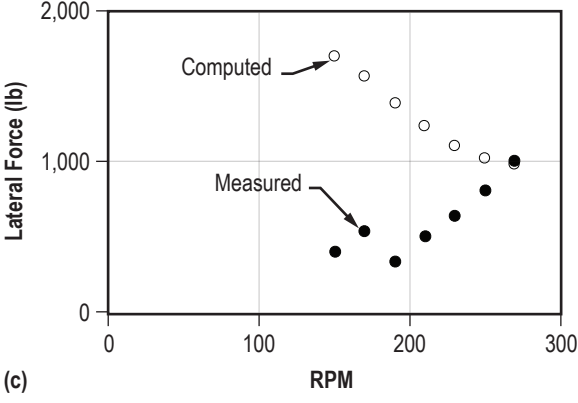
A comparison of computation and measurement for example is shown in figure 15.



(a)



(b)



(c)

Figure 15. Example 1 comparison of computation and measurement for 0.5-in-diameter pin and 1.2-in-diameter shoulder in 2219-T87 aluminum alloy for 8 in/min and 150 to 270 RPM: (a) Torque shows agreement in trend and magnitude, (b) drag shows agreement in trend, but computation overestimates drag, and (c) lateral force computation overestimates force and shows trend opposite to measurement.

4.7.2 Example 2

For a pin radius, $R=0.094$ and length, $w=0.125$, a shoulder radius, $R_s=0.2375$, estimating $R_o/R \approx 5$, and for 2195-T87 weld metal, it is possible to evaluate equations (45), (46), and (47).

For 2219-T87 aluminum alloy, $\rho C(T_{\text{melt}}-T_o)$ has the dimensions of a stress, about 185,100 psi, and $k/\rho C$ is a thermal diffusivity, about $0.530 \text{ cm}^2/\text{s}$.

The cross-sectional area of the tool, $2Rw=0.0235 \text{ in}^2$, when multiplied by the characteristic stress $\rho C(T_{\text{melt}}-T_o) \approx 185,100 \text{ psi}$, yields a force of 4,350 lb. The pin surface area times its radius, $2\pi R^2w=0.00694 \text{ in}^3$ when multiplied by the characteristic stress, yields a torque of 1,285 in-lb.

The angular velocity in radians per minute is $\omega=2\pi \cdot \text{RPM}$. If weld speed, V , is measured in inches per minute, then

$$\frac{V}{R\omega} = \frac{V}{2\pi R \cdot \text{RPM}} \approx 0.6366 \frac{V}{\text{RPM}} \quad (53)$$

is a dimensionless number. Similarly dimensionless is

$$\frac{\frac{k}{\rho C}}{R^2\omega} = \frac{\frac{k}{\rho C}}{2\pi R^2 \text{RPM}} = \frac{\left[0.530 \frac{\text{cm}^2}{\text{s}}\right] \left[\frac{1}{2.54} \frac{\text{in}}{\text{cm}}\right]^2 \left[60 \frac{\text{s}}{\text{min}}\right]}{2\pi [0.094 \text{ in}]^2 \left[\text{RPM} \frac{1}{\text{min}}\right]} = \frac{88.78}{\text{RPM}} \quad (54)$$

The moment, M , would be minimized by a very large value for n , but observations suggest values of 2 or 4 would more realistically describe the shape of the shear surface. If a value of $n=4$ is taken, the resulting moment and force computations become:

$$M \approx \left[\frac{114,080}{\text{RPM}} \text{ in-lb} \right] \left[\int_0^1 \frac{d\zeta}{\ln \frac{5}{1+1.527\zeta^4}} + 0.467 \right] \approx \frac{140,200}{\text{RPM}} \text{ in-lb} \quad , \quad (55)$$

$$F_{-x} \approx [4,350 \text{ lb}] \frac{V}{\text{RPM}} \cdot \int_0^1 \left[\frac{\pi}{\sqrt{1+21.09\zeta^6}} - \frac{1}{[1+1.526\zeta^4]^2} \ln \frac{5}{1+1.526\zeta^4} \frac{88.78}{\text{RPM}} \right] d\zeta$$

$$\approx 10,050 \frac{V}{\text{RPM}} \cdot \left(1 - \frac{18.94}{\text{RPM}} \right) \text{ lb} , \quad (56)$$

and

$$F_{-y} \approx [4,350 \text{ lb}] \frac{V}{\text{RPM}} \int_0^1 \left[\frac{\pi}{(1+1.527\zeta^4)^2} \ln \frac{5}{1+1.527\zeta^4} \sqrt{1+21.09\zeta^6} \frac{88.78}{\text{RPM}} + 1 \right] d\zeta$$

$$\approx 4,350 \frac{V}{\text{RPM}} \left(1 + \frac{30.13}{\text{RPM}} \right) \text{ lb} . \quad (57)$$

A comparison of computation and measurement for example 2 is shown in figure 16.

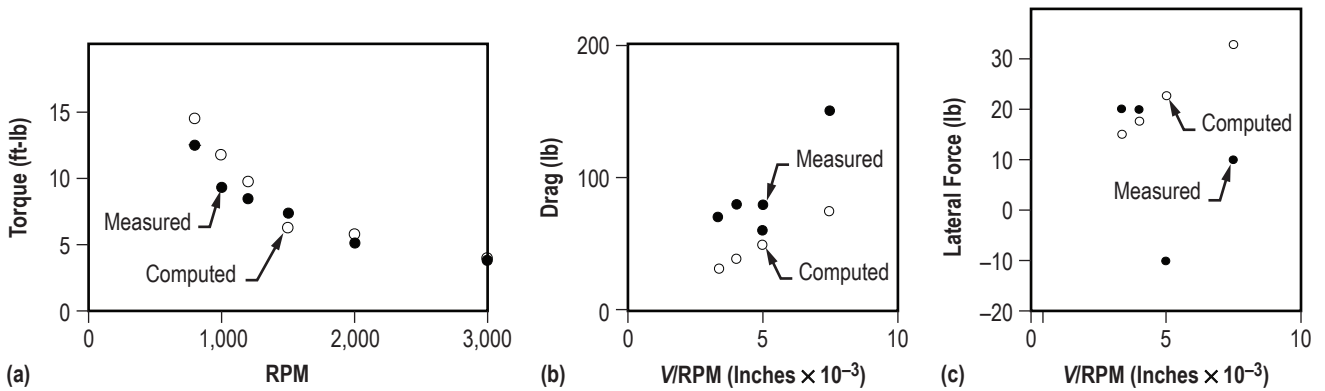


Figure 16. Example 2 comparison of computation and measurement for 0.19-in-diameter pin and 0.48-in-diameter shoulder in 2219-T87 aluminum alloy for 4 to 15 in/min and 800 to 3,000 RPM: (a) Torque shows agreement in trend and magnitude, (b) drag shows agreement in trend, but computation underestimates drag, and (c) lateral force computation is of similar magnitude to measurements, but measurements are erratic, even reversing sign, and do not show a definite trend for comparison.

4.7.3 Comments

Considering the rough approximations involved in the computations, the computed torque agrees well with the measurements in the examples. Still more approximations are included in the drag and lateral force computations.

The temperature variation over the shear surface is approximated by splitting the local conducting environment into ‘independent’ sectors, whose surface temperatures vary to accommodate the power that must be dissipated from each location on the shear surface. Although this method is crude, it does yield variations that seem to correspond to measured patterns⁵ and the torque computations, which are based on an average of these variations, do seem to agree with measured results.

The temperature variation estimate is then used to estimate the pressure variation over the shear surface. Within the large uniform pressure impinging upon the shear surface in reaction to the down-thrust of the plunge force on the tool is assumed a local pressure drop at the shear surface as the weld metal collapses into the metal plug rotating with the tool. This pressure drop is estimated as that to rotate a shear surface by 90° in analogy to that to rotate a shear surface by 180° for indenting a surface. This pressure drop amounts to $\pi\tau$, where τ is the temperature-dependent shear stress at that location. Reducing the factor π could bring the drag computation in line with the measured data in example 1, or raising it in example 2.

Drag computation is of the observed order of magnitude but overestimates drag by factors of $\times 1.9$ to $\times 3.1$ for example 1 and underestimates drag by factors of $\times 0.47$ to $\times 0.83$ for example 2. The computed trend follows the empirical trend. Minor conceptual revision of this model would seem to be needed.

Lateral force computations ran from 0.97 to 4.3 times measured forces in example 1 and 0.75 to 3.3 times measured forces in example 2, with some measured values negative. Although the computations are of the order of magnitude of the observed values, the computed trends did not follow measured trends, which appeared to be somewhat erratic and, in the case of example 2, exhibit negative values.

This suggests that drag and lateral forces are sensitive to features beyond those included in the computations, perhaps to tool lead angle and plunge force (or depth setting) effects on flow phenomena at the pin bottom or the shoulder edge, or perhaps to pin thread or shoulder scroll geometry effects upon the circulation of weld metal adjacent to the tool.

4.8 Force Variations

Friction stir forces exhibit variations that superimpose over the basic steady state effects described above. A rise in workpiece temperature may be expected to produce a downward drift in torque and forces, although if the tool sinks deeper into the workpiece, interactions at the anvil and the buried edge of the shoulder may complicate things. If these complications are ignored, drift effects may be approximated by varying the ambient temperature.

Small periodic variations¹⁷ in torque and, more clearly, plunge force (in position control mode) as shown in figure 17 correlate with the positions of the clamps holding the weld metal and can be interpreted as due to local temperature variation.

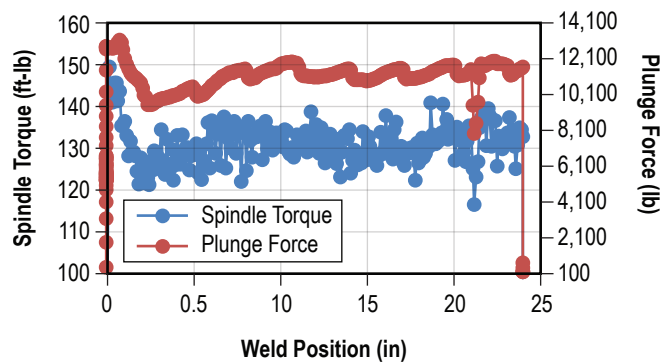


Figure 17. Torque and plunge force variation with position of tool along weld in 0.327-in-thick, 2195-T81 aluminum alloy. Vertical lines mark 1.5-in-wide gaps between 4.5-in-wide clamps. Welds were made at 200 RPM and 6 in/min. A 0.311-in-long, 1/2-20 UNJF threaded pin was used with a smooth 1.2-in-diameter shoulder.¹⁷

4.9 Force Oscillations

The effect of tool eccentricity on surface ripples and internal textural banding in the wake of the friction stir tool is discussed in section 2.5. Force oscillations with the same period as that of the tool rotation accompany the production of these structural features.

The eccentric displacement forces appear as a high-frequency perturbation superposed on the drag, lateral, and plunge forces. The tool rotation frequency is too high to be resolved with the available force measuring instrumentation. Hence, the oscillation forces appear¹⁶ as random force variations along the mean force as shown in figure 18.

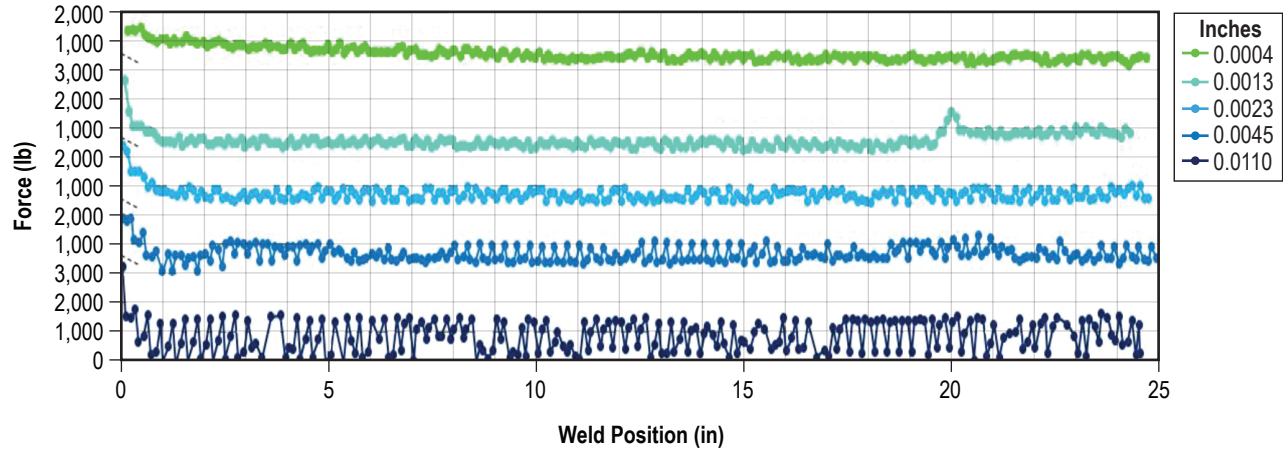


Figure 18. Drag or plow force variation with position of tool along weld in 0.327-in-thick, 2219-T87 aluminum alloy. From top to bottom, each curve represents a weld made at a different preweld eccentricity: 0.0004 in, 0.0013 in, 0.0023 in, 0.0045 in, and 0.0110 in. Welds were made at 220 RPM and 6 in/min with a 2.5° lead angle. A 1/2-20 UNJF threaded pin was used with a smooth 1.2-in-diameter shoulder.¹⁶

Empirical sinusoidal force amplitudes were estimated at $\sqrt{2}$ times the standard deviation of the variations. (Amplitudes of a triangular or sawtooth wave would be $\sqrt{3}$ times the standard deviation of the variations.)

$$\text{Standard deviation} = \sqrt{\frac{\int_0^{2\pi} \delta^2 \sin^2 \theta d\theta}{2\pi}} = \frac{\delta}{\sqrt{2}}. \quad (58)$$

The dependence of the drag or plow force and the lateral force on tool preweld eccentricity are shown in figure 19.

Judging from the small ripple magnitude, the FSW pin is very little displaced with respect to the workpiece during an oscillation. This implies that the tool eccentricity is almost wholly accommodated by elastic deformation of the tool. One would anticipate force amplitudes to be equal to the product of machine stiffness times the tool eccentricity minus a small relaxation due to deformation of the weld metal, but a preliminary study²¹ does not confirm this expectation. Estimates of oscillation force amplitudes compared to measured values are tabulated in table 3.

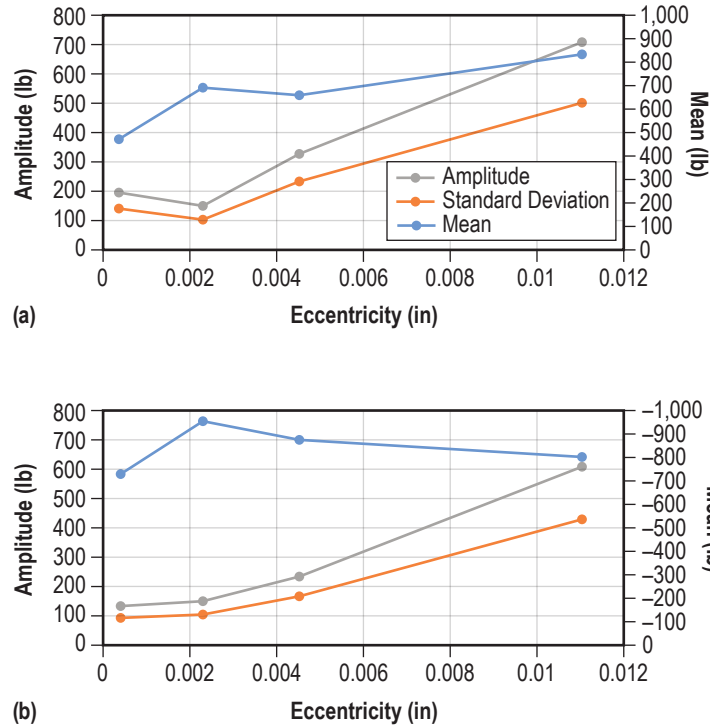


Figure 19. Tool preweld eccentricity effect: (a) Drag or plow force variation and (b) lateral or side force variation with tool eccentricity. Variations appear roughly the same, suggesting a force rotating with the tool.¹⁶

Table 3. Comparison of estimated and measured oscillation amplitudes of drag and lateral forces.²¹

	FSW Machine No. 1	FSW Machine No. 1	FSW Machine No. 2
Measured tool eccentricity, ε (in)	0.004	0.001	0.001
Measured machine spring constant in drag direction k_x (lb/in)	59,000	59,000	67,000
Estimated drag oscillation amplitude, $k_x \varepsilon$ (lb)	236	59	67
Measured drag oscillation amplitude, ΔF_x (lb)	579	85	301
Measured machine spring constant in lateral direction, k_y (lb/in)	32,000	32,000	50,000
Estimated lateral force oscillation amplitude, $k_y \varepsilon$ (lb)	128	32	50
Measured lateral force oscillation amplitude, ΔF_y (lb)	713	194	255

The estimated drag and lateral force amplitudes consistently and substantially underestimate the measured values as if there is an unaccounted for latent eccentricity. Such latent eccentricities are estimated in table 4. They range from 0.09 to 4.26 times the offset between tool and shear surface rotation axes as shown in figure 3, $V / \omega = 6 \frac{\text{in}}{\text{min}} / 220 \frac{\text{rev}}{\text{min}} 2\pi \frac{\text{rad}}{\text{rev}} = 0.0043$ inches. No relation between latent eccentricity and shear surface eccentricity is apparent. Further, the shear surface eccentricity is fixed with respect to the workpiece and results in a steady lateral force, not an oscillating force. Lateral force computations above take this force into account.

Table 4. Latent eccentricity that, added to measured tool eccentricity, would bring force oscillation estimates equal to measurements.

	FSW Machine No. 1 (in)	FSW Machine No. 1 (in)	FSW Machine No. 2 (in)
Drag	0.0058	0.0004	0.0035
Lateral force	0.0183	0.0051	0.0041

The dynamic spring constant could perhaps be greater than the static value. (The spring constant was taken as the slope of the force-displacement curve at the mean drag or lateral force, so that a nonlinear force-displacement relation would not cause a large error.) A resonance effect increasing the effective force is thought to be unlikely and would presumably be noticeable if it existed. For the present, these discrepancies are unexplained.

5. SUMMARY

The main features of the FSW structure appear to be well understood.

The metallic bond and the consequent metallic crystal structure with its characteristic deformation mechanisms results in a metal flow stress that is only weakly dependent upon the shearing deformation rate of the metal. As a result, at high deformation rates, the region of plastic flow tends to contract into narrow 'adiabatic shear bands.' In FSW, the main shear deformation tends to take place at a narrow shear surface encapsulating the weld tool. The shear surface separates a plug of weld metal that sticks to the tool from the stationary weld metal bulk adjacent to the tool. The shear surface plays a dominant role in determining the weld structure.

As the tool moves along the weld seam, metal intercepted on the leading surface of the tool enters the rotating plug through the shear surface, is rotated to the trailing surface, and is released through the shear surface into the wake of the tool. Passage through the violent shearing at the shear surface results in recrystallized weld nugget material.

Relatively slow auxiliary bulk deformation of the hot weld metal near the tool distorts the weld nugget. Threads on the FSW pin, scrolling on the tool shoulder, or a tool lead angle induce flow along the tool surface and set up a ring vortex circulation around the tool. Radial components of this flow across the shear surface can delay or prematurely release metal from the rotating plug so as to cause substantial lateral shifts in flow streamlines. The same ring vortex flow may also entrain surface contaminants into the interior of the weld.

FSW tool eccentricity periodically squeezes and releases the hot metal along the shear surface so as to cause a periodic outflow and inflow of surface ripples trailing the weld as well as a periodic internal textural banding visible as the onion ring pattern on transverse weld sections.

The FSW torque, drag, and lateral forces can be estimated using a simplified approach based upon an estimate of the temperature variation over the shear surface. Given the local temperature, the local torque can be estimated and integrated over the shear surface to yield a torque. Although a number of simplifying approximations are incorporated into the computation, no general fudge factors were used, and for two sample cases, the computed torques were in good agreement with observed values.

In order to compute the FSW tool drag force a mechanism for incorporating weld metal into the rotating plug through the shear surface was hypothesized. The pressure variation over the shear surface was estimated from the local shear stress and the angle of bending of a weld metal streamline at the site. The drag was estimated from integrating local pressure and shear contributions over the shear surface. The computed variation trends agreed with observations, but the estimated magnitudes were too big for one example and too small for the other.

A lateral force can be estimated by integrating lateral force contributions from the local pressure and shear stress. The computations agreed with observations in order of magnitude, but not in variational trends.

Slow variations in torque and forces along the weld seam are observed. These appear to be due to temperature variations. Variations correlating with hold-down clamp positions are observed. Slower variations are assumed due to weld thermal transients. Rapid fluctuations in forces at the rotation period of the tool are caused by tool eccentricity.

A number of questions remain. Why the discrepancy in drag force computation? Could it be due to an error in the estimate of pressure variation around the circumference of the shear surface? Why the discrepancy in lateral force computation? Could it be due to neglect of anvil interactions? Why is not the force oscillation amplitude limited by the elastic constant of the tool times the eccentricity?

The above study lays a groundwork for but does not address the important question of the relation of the resultant weld structures to strength and of defect formation. It is hoped to take up the complex study of strength variations and of defect formation in friction stir welds in a subsequent project.

The emphasis here has been upon understanding. Understanding takes place through concepts appropriate to the scale of the system to be understood. The building blocks of the present theory are concepts derived from plasticity theory, hypothetical flow components into which the flow may be decomposed. The emphasis has not been on precise computation and approximations have been ubiquitous. The objective was to obtain a small set of simple concepts that would explain FSW structures and forces. On the whole, it is judged that the objective was met, but questions remain. It is anticipated that the questions can be resolved and model verisimilitude enhanced to the degree desired by modifying and extending concepts in accordance with clues provided by remaining disparities between computations and measurements.

APPENDIX A—SHEAR SURFACE WIDTH

If the flow stress of a metal is insensitive to the rate of deformation, then a very steep drop in deformation rate is required to maintain equilibrium and plastic flow at the same time. In the case of a friction stir weld, the drop in angular velocity from that of the pin to zero in the weld metal plate takes place within a very short distance. The width of the (rapid) shear zone about the tool (ignoring a relatively slow parallel flow) is narrow enough to be treated as a surface. It is possible to illustrate how this occurs in a simplified model and to estimate temperature and velocity distributions within the shear surface as well as the width of the shear surface.

A simplified model of the shear surface comprising a shearing column of metal extended in the y -direction with the bottom at $y=0$ fixed and the top made to move at velocity V , is shown in figure 20. The bottom of the column is insulated and the heat generated by plastic deformation is conducted away through the column in the y -direction. Hence, the temperature drops along the column. It is hotter and the flow stress is less at the bottom of the column. Shear deformation takes place at the bottom of the column to compensate for the drop in flow stress due to the rise in temperature so as to maintain equilibrium. When the velocity increments due to the flow add up to V , plastic flow stops, no further heat is generated, and the flow stress, now larger than the acting stress, rises as the temperature declines as required for heat outflow.

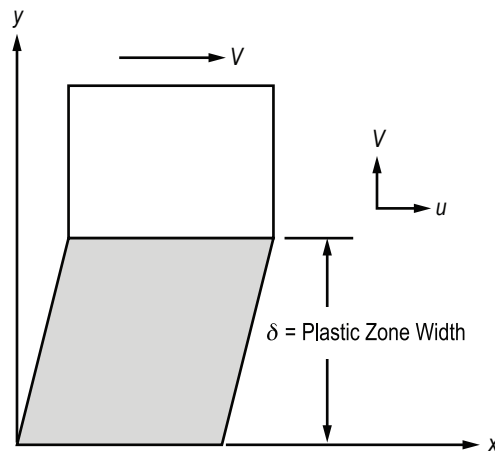


Figure 20. A simplified model of the shear surface comprising a shearing column of metal extended in the y -direction with the bottom at $y=0$ fixed and the top made to move at velocity V .

Equilibrium requires that the shear stress, τ , remain constant along the column:

$$\frac{\partial \tau}{\partial y} = 0. \quad (59)$$

A constitutive relation for the weld metal is symbolized by

$$\frac{\partial \tau}{\partial y} = \frac{\partial \tau}{\partial T} \frac{\partial T}{\partial y} + \frac{\partial \tau}{\partial \dot{\gamma}} \frac{\partial \dot{\gamma}}{\partial y}. \quad (60)$$

Compatibility of strain rate $\dot{\gamma}$ with flow field $u(y)$ requires

$$\dot{\gamma} = \frac{\partial u}{\partial y}. \quad (61)$$

The heat conduction equation maintains conservation of energy:

$$\frac{\partial}{\partial y} \left(-k \frac{\partial T}{\partial y} \right) = \tau \frac{\partial u}{\partial y}. \quad (62)$$

where k is the thermal conductivity of the weld metal and T is the temperature. Taking k as a constant,

$$\frac{\partial^2 T}{\partial y^2} = -\frac{\tau}{k} \frac{\partial u}{\partial y}. \quad (63)$$

Combining equations (59), (60), and (61), and taking $(-\partial\tau/\partial T)$ and $(\partial\tau/\partial\dot{\gamma})$ as constant,

$$\frac{\partial T}{\partial y} = \frac{\left(\frac{\partial \tau}{\partial \dot{\gamma}} \right)}{\left(-\frac{\partial \tau}{\partial T} \right)} \frac{\partial^2 u}{\partial y^2} \quad (64)$$

and

$$\frac{\partial^2 T}{\partial y^2} = \frac{\left(\frac{\partial \tau}{\partial \dot{\gamma}} \right)}{\left(-\frac{\partial \tau}{\partial T} \right)} \frac{\partial^3 u}{\partial y^3}. \quad (65)$$

Inserting equation (63) into equation (65):

$$\frac{\partial^3 u}{\partial y^3} + \frac{\tau \left(-\frac{\partial \tau}{\partial T} \right)}{k \left(\frac{\partial \tau}{\partial \dot{\gamma}} \right)} \frac{\partial u}{\partial y} = 0 . \quad (66)$$

Equation (66) can be solved by substituting a solution of sinusoidal form and fitting it to the boundary conditions, $u(0) = 0$ and $u(\delta) = V$:

$$u = V \sin \frac{\pi y}{2 \delta} \quad (67)$$

and

$$\delta = \frac{\pi}{2} \sqrt{\frac{k \left(\frac{\partial \ln \tau}{\partial \dot{\gamma}} \right)}{\left(\frac{\partial \tau}{\partial T} \right)}} . \quad (68)$$

If the flow stress of an alloy is completely insensitive to strain rate ($\partial \ln \tau / \partial \dot{\gamma} = 0$), then the width of the shear surface, δ , is zero. The temperature variation is given by

$$T = T(y=0) - \frac{\tau V}{k} \frac{2\delta}{\pi} \left(1 - \cos \frac{\pi y}{2 \delta} \right) . \quad (69)$$

It satisfies the boundary conditions $\left. \frac{\partial T}{\partial y} \right|_{y=0} = 0$ and $\left. \frac{\partial T}{\partial y} \right|_{y=\delta} = -\frac{\tau V}{k}$. The temperature drop, ΔT , across the shear surface is

$$\Delta T = -\frac{\tau V}{k} \frac{2\delta}{\pi} . \quad (70)$$

For 2219-T87 aluminum alloy, $k/(-\partial \tau / \partial T) \approx 4.89 \text{ in}^2/\text{s}$. A value of $(\partial \ln \tau / \partial \dot{\gamma})$ is estimated from experimental data reported in the literature. If shear stress τ_1 is measured at strain rate $\dot{\gamma}_1$ and τ_2 at $\dot{\gamma}_2$, then

$$\left(\frac{\partial \ln \tau}{\partial \dot{\gamma}} \right) \approx \frac{\ln \frac{\tau_1}{\tau_2}}{\dot{\gamma}_1 - \dot{\gamma}_2} . \quad (71)$$

The properties $(-\partial \tau / \partial T)$ and $(\partial \ln \tau / \partial \dot{\gamma})$ are structure and temperature dependent, but the values pertinent to FSW are those at high temperatures, where the metal is substantially softened and precipitation and work hardening structures tend to be dissolved. Reference 22 exhibits shear stress versus shear strain curves for a commercially pure aluminum alloy. Extrapolating to a maximum reported strain of 40%, the stress rises from about 77 to 80 ksi as the shear strain rate rises from

2,200 to 2,800 s⁻¹. This suggests a $(\partial \ln \tau / \partial \dot{\gamma})$ on the order of 0.00006 s. With these values, equation (68) estimates a shear surface width δ of 0.027 inches. This is much larger than the observed width of the boundary between the parent metal and the refined nugget material as shown in figure 1. It should be noted, however, that the nugget/parent metal boundary could be narrower than the shear zone if recrystallized metal consumes part of the shear zone.

If the heat is not removed by conduction, but by convection, to a metal flow downward through the column at velocity W , the heat transfer equations (62) and (63) become, respectively, equations (72) and (73):

$$-\rho CW \frac{\partial T}{\partial y} = \tau \frac{\partial u}{\partial y} \quad (72)$$

and

$$\frac{\partial T}{\partial y} = -\frac{\tau}{\rho CW} \frac{\partial u}{\partial y} \quad (73)$$

Taking $(-\partial \tau / \partial T)$ and $(\partial \tau / \partial \dot{\gamma})$ as constant, equation (64) becomes equation (74):

$$\frac{\partial^2 u}{\partial y^2} + \frac{\tau}{\rho CW} \frac{\left(-\frac{\partial \tau}{\partial T}\right)}{\left(\frac{\partial \tau}{\partial \dot{\gamma}}\right)} \frac{\partial u}{\partial y} = 0 \quad (74)$$

Equation (74) can be solved by substituting a solution of exponential form and fitting it to the boundary conditions, $u(0) = 0$ and $u(\delta) = V$, with the following result:

$$u = V \frac{1 - e^{-\frac{y}{\delta}}}{1 - e^{-\frac{\delta}{\rho CW \frac{\left(\frac{\partial \ln \tau}{\partial \dot{\gamma}}\right)}{\left(-\frac{\partial \tau}{\partial T}\right)}}}} \quad (75)$$

The shear surface width, δ , in equation (75) is determined by wherever the velocity, V , is applied to the column; however the characteristic distance $\rho CW \frac{(\partial \ln \tau / \partial \dot{\gamma})}{(-\partial \tau / \partial T)}$ is a property of the system and constitutes a rough measure of the effective surface width:

$$\delta \sim \rho CW \frac{\left(\frac{\partial \ln \tau}{\partial \dot{\gamma}} \right)}{\left(-\frac{\partial \tau}{\partial T} \right)}. \quad (76)$$

For an aluminum alloy like 2219 aluminum,

$$\delta(\text{in}) \sim 0.00006 \cdot W(\text{in/min}). \quad (77)$$

This suggests that for a weld speed of 5 in/min, a shear surface width of the order of 0.0003 in would be anticipated at the weld centerline dominated by convection effects. At the weld edges, the convection effect would disappear and conduction would limit the shear surface width to the order of 0.027 in.

These results should be regarded as speculative; they are based upon poorly known physical properties. Additional features affecting the shear surface, for instance, the dynamic force as the weld metal is accelerated and decelerated by the weld tool or the curvature of the shear surface, have been ignored here. A cursory inspection of figure 1 suggests a shear surface width of the order of 0.001 in, at least an order of magnitude smaller than the 0.027 in computed magnitude.

APPENDIX B—SHEAR SURFACE POSITION

The shear surface of the partial penetration weld bead shown in figure 21 does not hug the bottom of the pin, but extends between the pin bottom and the anvil. The location of the shear surface between pin and anvil is of practical significance. It is impossible to set the pin bottom exactly on the anvil as there must always be a small clearance between the pin bottom and the anvil. This clearance has sometimes been called the ‘ligament.’ If the shear surface extends all the way to the anvil, the weld extends all the way to the anvil. If not, penetration is incomplete and weld strength is reduced.

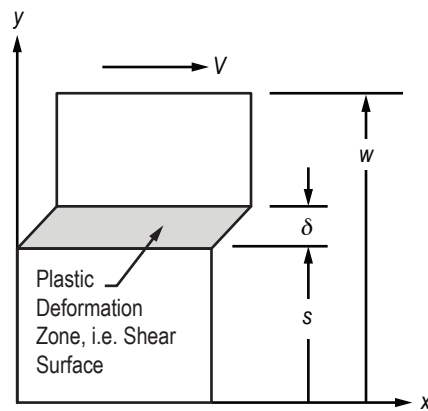


Figure 21. A simplified model of the shear surface comprising a shearing column of metal extended in the y -direction with the bottom at $y=0$ fixed and the top made to move at velocity, V . The shear surface is located between $y=s$ and $y=s+\delta$. The location of the shear surface, s , depends upon the boundary conditions at $y=0$ and $y=w$.

In the computation of the shear surface width of appendix A, at $y=0$ no heat outflow is assumed. The temperature there rises to a maximum, and this is where plastic deformation begins. From here, the temperature drops with increasing y until conditions for plastic deformation are no longer met.

If the heat generated in the plastic deformation zone is conducted away at both $y=0$ and $y=w$, the zero heat flow condition of appendix A occurs at an intermediate position at $s < y < s + \delta$, where the heat flow divides in two, a forward and a backward flow. If $\delta \ll s$, then the shear surface is located at s , which may be estimated assuming that the shear surface location minimizes the shear stress required for the deformation. The temperature at s is taken to be T . The thermal conductivity is assumed to be k , uniform throughout. The boundary temperatures are taken to be fixed at $T(0)$ at $y=0$ and $T(w)$ at $y=w$.

$$\tau V \approx k \frac{T - T(0)}{s} + k \frac{T - T(w)}{w - s}, \quad (78)$$

$$\frac{\partial \tau}{\partial s} \approx \frac{k}{V} \frac{\partial}{\partial s} \left(\frac{T - T(0)}{s} + \frac{T - T(w)}{w - s} \right) = 0, \quad (79)$$

and

$$\frac{T - T(w)}{T - T(0)} \approx \left(\frac{w}{s} - 1 \right)^2. \quad (80)$$

The shear surface tends to move toward the hotter bounding surface. In the case of figure 21, the location of the shear surface, very roughly a third of the distance between the pin and anvil, implies that the anvil temperature, $T(w)$ is less than the pin temperature, $T(0)$:

$$\left(\frac{T - T(w)}{T - T(0)} \right) \approx 4. \quad (81)$$

If the shear surface temperature were 450 °C, and the pin were 30 °C cooler, the anvil temperature would be 120 °C cooler, or 330 °C. If the anvil were brought closer to the pin so that its temperature was to approach the pin temperature, then the shear surface would approach the midpoint between the pin and anvil. If the anvil were insulated so that its temperature could approach that of the shear surface, the shear surface would approach the anvil.

The situation determining the lateral position of the shear surface is different. Instead of a balance of heat flows from the shear surface to two heat-sinking surfaces, the heat flow is taken to be entirely radially outward from the lateral shear surface into a conductive sector of the weld metal as described in section 3.1. Using this model, the temperature distribution over the shear surface was estimated:

$$(T - T_o) = \frac{1}{\frac{1}{\ln \frac{R_o}{r}} \left(\frac{k}{r^2 \omega \rho C} \right) + \frac{V}{r \omega} \cos \theta} (T_{\text{melt}} - T_o). \quad (82)$$

$$1 + \frac{1}{\frac{1}{\rho C} \left(-\frac{\partial \tau}{\partial T} \right) \sqrt{1 + \left(\frac{dr}{dz} \right)^2} \left(1 + \frac{V}{r \omega} \sin \theta \right)}$$

As the RPM, equivalently ω , increases and the shear surface temperature, T , approaches the melting temperature, T_{melt} , of the weld metal, the effect of radius on shear surface temperature approaches zero. For a first approximation to the lateral contour of the shear surface, the shear surface temperature is taken as constant and its position determined by selecting the contour that minimizes torque.

APPENDIX C—LATERAL CONTOUR OF ISOTHERMAL SHEAR SURFACE

The shear surface as sketched in figure 2 encloses the plug of metal that rotates with the FSW tool. The shear surface is not constrained to follow the tool weld metal interface as a slip surface would be. The favored shear surface configuration would be that for which the tool turns most easily, i.e., the configuration minimizing torque. The shear surface is taken to conform to a flat pin bottom, but the lateral shear surface contour $r(z)$ is taken to be determined by minimizing torque over the shear surface. The torque is estimated in equation (83): shear stress times area times moment arm integrated over the shear surface. Shear stress circumferential variations are ignored in equation (83):

$$M \approx \int_{z=0}^{z=w} \left[\tau(2\pi r) \sqrt{dz^2 + dr^2} \right] r = \int_{z=0}^{z=w} 2\pi r^2 \tau \sqrt{1 + \dot{r}^2} dz. \quad (83)$$

The shear surface contour is determined by an exercise in calculus of variations represented by equation (84):

$$\delta \int_{z=0}^{z=w} 2\pi r^2 \tau \sqrt{1 + \dot{r}^2} dz \approx 0. \quad (84)$$

For an isothermal shear surface, equivalently a constant shear stress, τ , surface, equation (84) implies the Euler equation:

$$\frac{d}{dz} \left[\frac{\partial}{\partial \dot{r}} \left(r^2 \sqrt{1 + \dot{r}^2} \right) \right] - \frac{\partial}{\partial r} \left(r^2 \sqrt{1 + \dot{r}^2} \right) \approx 0. \quad (85)$$

Note that $\dot{r} \equiv \frac{dr}{dz}$.

From equation (84), the differential equation for the shear surface radius, r , as a function of depth, z , is obtained:

$$\ddot{r} - \frac{2}{r} (1 + \dot{r}^2) \approx 0. \quad (86)$$

The boundary conditions are $r(0) = R$ and $r(w) = R_s$.

Equation (86) is a rough approximation and does not merit an extremely precise solution. Integration is done by a finite difference approximate piece-by-piece buildup:

$$r_{i+1} = r_i + \dot{r}_i \Delta z, \quad (87)$$

$$\dot{r}_{i+1} = \dot{r}_i + \ddot{r}_i \Delta z, \quad (88)$$

and

$$\ddot{r}_{i+1} \approx \frac{2}{r_i} (1 + \dot{r}_i^2). \quad (89)$$

The initial \dot{r} is estimated by trial and error to yield $r(w)$. This is illustrated by an example where pin radius $R=0.25$ in, shoulder radius $R_s=0.75$ in, and pin length $w=0.25$ in (table 5).

Table 5. Various estimates of the shear surface contour for pin radius, $R=0.25$ in; shoulder radius, $R_s=0.75$ in; and pin length, $w=0.25$ in.

					$r \approx R + (z/w)^n (R_s - R)$	
i	\ddot{r}_i	\dot{r}_i	r_i	z_i	$r(n=2)$	$r(n=4)$
0	-	1	0.25	-	0.250	0.250
1	16	1	0.300	0.050	0.270	0.251
2	13.33	1.8	0.350	0.100	0.330	0.263
3	24.23	2.467	0.440	0.150	0.430	0.315
4	-	3.679	0.563	0.200	0.570	0.455
5	-	-	0.747	0.250	0.750	0.750

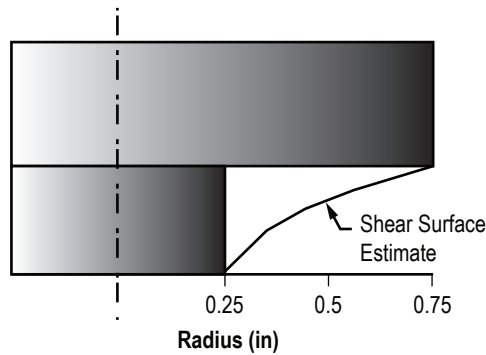


Figure 22. Approximate shear surface lateral contour from simplified computation. Compare with apparent contours of figures 8 and 9.

A convenient, simple expression for the shear surface contour is used in equation (43):

$$r - R \approx \left(\frac{z}{w} \right)^n (R_s - R) .$$

The expression is compared with the approximate numerically computed values in table 5. It satisfies the differential equation:

$$\ddot{r} - \left(1 - \frac{1}{n} \right) \frac{\dot{r}^2}{(r - R)} \approx 0 . \quad (90)$$

The observed shear surface contours of figure 21 appear to have a steeper initial slope than this computation, hence, the $n=4$ representation is used although it does not agree as well with the sample computation as the $n=2$ representation. The initial slope of the sample computation also becomes steeper when more points are used.

APPENDIX D—COMPARISON OF COMPUTATIONS WITH MEASURED FORCES

A comparison of computations with measured forces for example 1 is given in table 6 (courtesy of Z.S. Courtright, MSFC) and for example 2 in table 7 (courtesy of R. Carter, MSFC).

Table 6. Comparison of computations with measured forces—example 1.

RPM	Measured Torque (ft-lb)	Computed Torque (ft-lb)
150	174	201 (×1.2)
170	158	177 (×1.1)
190	158	159 (×1)
210	147	144 (×0.98)
230	137	131 (×0.96)
250	128	121 (×0.95)
270	121	112 (×0.93)

RPM	Measured Drag (lb)	Computed Drag (lb)	Measured Lateral Force (lb)	Computed Lateral Force (lb)
150	1,889	3,667 (×1.9)	418	1,803 (×4.3)
170	1,662	3,242 (×2)	560	1,569 (×2.8)
190	1,423	2,906 (×2)	353	1,389 (×3.9)
210	963	2,633 (×2.7)	512	1,245 (×2.4)
230	780	2,407 (×3.1)	650	1,128 (×1.7)
250	811	2,216 (×2.7)	811	1,032 (×1.3)
270	679	2,054 (×3)	1,012	982 (×0.97)

Table 7. Comparison of computations with measured forces—example 2.

RPM/IPM	Measured Torque (ft-lb)	Computed Torque (ft-lb)
800/4	12.5	14.6 ($\times 1.17$)
1,000/4	9.25	11.7 ($\times 1.26$)
1,200/4	8.5	9.7 ($\times 1.14$)
1,500/6	6.3	7.8 ($\times 1.24$)
2,000/15	5.25	5.8 ($\times 1.1$)
3,000/15	3.8	3.9 ($\times 1.03$)

RPM/IPM	Measured Drag (lb)	Computed Drag (lb)	Measured Lateral Force (lb)	Computed Lateral Force (lb)
800/4	80	49 (0.61)	-10	23 (??)
1,000/4	80	39 (0.49)	20	18 (0.9)
1,200/4	70	33 (0.47)	20	15 (0.75)
1,500/6	80	40 (0.5)	20	18 (0.9)
2,000/15	150	75 (0.5)	10	33 ($\times 3.3$)
3,000/15	60	50 (0.83)	-10	22 (??)

REFERENCES

1. Thomas, W.M.; et al. "Friction Stir Butt Welding," International Patent Application No. PCT/GB92/02203 and GB Patent Application No. 9125978.8, December 1991.
2. Colligan, K.: "Material Flow Behavior during Friction Stir Welding of Aluminum," *Welding Journal*, Vol. 78, No. 7, pp. 229-s to 237-s, 1999.
3. Reynolds, A.P.; Seidel, T.U.; and Simonsen, M.: "Visualization of Material Flow in an Autogenous Friction Stir Weld," 1st International Symposium on Friction Stir Welding, Rockwell Science Center, Thousand Oaks, CA, June 14–16, 1999.
4. Schneider, J.; Brooke, S.; and Nunes, Jr., A.C.: "Material Flow Modification in a FSW Through Introduction of Flats," *Metallurgical and Materials Transactions B.*, Vol. 47, No. 1, pp. 720–730, 2016.
5. Fehrenbacher, A.; Schmale, J.R.; Zinn, M.R.; and Pfefferkorn, F.E.: "Measurement of Tool-Workpiece Interface Temperature Distribution in Friction Stir Welding," *Journal of Manufacturing Science and Engineering*, Vol. 136, pp. 021009-1 to 021009-8, 2014.
6. Nadai, A.: *Theory of Flow and Fracture of Solids*, Vol. 1, 2nd Edition, McGraw-Hill Book Company, Inc., p. 315, 1950.
7. Nunes, Jr., A.C.: "Prolegomena to the Study of Friction Stir Welding," Materials Science & Technology 2010 Conference and Exhibition, Houston, TX, October 17–21, 2010.
8. Nunes, Jr., A.C.: "Flow in the Proximity of the Pin-Tool in Friction Stir Welding and Its Relation to Weld Homogeneity," Preprint, 37th Annual Technical Meeting of the Society of Engineering Science, University of South Carolina, Columbia, SC, October 23–25, 2000.
9. Heurtier, P.; Jones, M.J.; Desrayaud, C.; et al.: "Mechanical and Thermal Modeling of Friction Stir Welding," *Journal of Materials Processing Technology*, p. 171, 348–357, 2006.
10. Leonard, A.J.; and Lockyer, S.A.: "Flaws in Friction Stir Welds," 4th International Symposium on Friction Stir Welding, Park City, UT, May 14–16, 2003.
11. Klages, H.K.: "The 'Lazy S' Feature in Friction Stir Welding of AA2099 Aluminum-Lithium Alloy," M.S. Thesis in Mechanical Engineering. Naval Postgraduate School, Monterey, CA, 2007.
12. Savolainen, K.: "Friction Stir Welding of Copper and Microstructure and Properties of the Welds," Doctoral Dissertation, School of Engineering, Aalto University, Espoo, Finland, 2012.

13. Nunes, Jr., A.C.; Russell, C.K.; Brooke, S.A.; et al.: "Laser Ablation Cleaning of Self-Reacting Friction Stir Weld Seam Surfaces: A Preliminary Evaluation," NASA/TM—2014–217500," NASA Marshall Space Flight Center, Huntsville, AL, 40 pp., February 2014.
14. Rubisoff, H.A.; Schneider, J.A.; and Nunes, Jr., A.C.: "Control of Structure in Conventional Friction Stir Welds through a Kinematic Theory of Metal Flow," *Friction Stir Welding and Processing-V*, R.S. Mishra, M.W. Mahoney, and T.J. Lienert (eds.), The Minerals, Metals & Materials Society, February 15–19, 2009, San Francisco, CA, pp. 149–158, 2009.
15. Galloway, L.: "Formation of Ripple Contours in Friction Stir Welding," NASA Summer Internship Final Report, NASA Marshall Space Flight Center, Huntsville, AL, 2013.
16. Tarwater, E.N.: "Effects of Pin Eccentricity on Friction Stir Welds," NASA Summer Internship Final Report, NASA Marshall Space Flight Center, Huntsville, AL, 2015.
17. McGroary, K.J.: "Temperature Variation in Friction Stir Welding (FSA)," NASA Summer Internship Final Report, NASA Marshall Space Flight Center, Huntsville, AL, 2001.
18. Sato, Y.S.; Park, S.H.C.; and Kokawa, H.: "Microstructural factors governing hardness in friction stir welds of solid-solution-hardened Al alloys," *Metallurgical and Materials Transactions A*, Vol. 32, No. 12, pp. 3033–3042, December 2001.
19. Hust, A.G.; and Lankford, A.B.: National Bureau of Standards, Thermal Conductivity of Aluminum, Copper, Iron, and Tungsten for Temperatures from 1K to the Melting Point, NBSIR 84-3007, June 1984.
20. Davis, J.R.: ASM Metals Handbook, Vol. 2, 10th Edition, 1998.
21. Sullivan, C.: "Effects of Machine Stiffness on Friction Stir Welds, NASA Summer Internship Final Report, NASA Marshall Space Flight Center, Huntsville, AL, 2016.
22. Tsao, M.C.; and Campbell, J.D.: "Plastic shear properties of metals and alloys at high strain rates," Air Force Materials Laboratory Report No. AFML-TR-73-177 distributed by National Technical Information Service, U.S. Department of Commerce, Springfield, VA, 1973.

REPORT DOCUMENTATION PAGE			Form Approved OMB No. 0704-0188		
<p>The public reporting burden for this collection of information is estimated to average 1 hour per response, including the time for reviewing instructions, searching existing data sources, gathering and maintaining the data needed, and completing and reviewing the collection of information. Send comments regarding this burden estimate or any other aspect of this collection of information, including suggestions for reducing this burden, to Department of Defense, Washington Headquarters Services, Directorate for Information Operation and Reports (0704-0188), 1215 Jefferson Davis Highway, Suite 1204, Arlington, VA 22202-4302. Respondents should be aware that notwithstanding any other provision of law, no person shall be subject to any penalty for failing to comply with a collection of information if it does not display a currently valid OMB control number.</p> <p>PLEASE DO NOT RETURN YOUR FORM TO THE ABOVE ADDRESS.</p>					
1. REPORT DATE (DD-MM-YYYY) 01-03-2018		2. REPORT TYPE Technical Memorandum		3. DATES COVERED (From - To)	
4. TITLE AND SUBTITLE Understanding Friction Stir Welding			5a. CONTRACT NUMBER		
			5b. GRANT NUMBER		
			5c. PROGRAM ELEMENT NUMBER		
6. AUTHOR(S) A.C. Nunes, Jr.			5d. PROJECT NUMBER		
			5e. TASK NUMBER		
			5f. WORK UNIT NUMBER		
7. PERFORMING ORGANIZATION NAME(S) AND ADDRESS(ES) George C. Marshall Space Flight Center Huntsville, AL 35812			8. PERFORMING ORGANIZATION REPORT NUMBER M-1456		
9. SPONSORING/MONITORING AGENCY NAME(S) AND ADDRESS(ES) National Aeronautics and Space Administration Washington, DC 20546-0001			10. SPONSORING/MONITOR'S ACRONYM(S) NASA		
			11. SPONSORING/MONITORING REPORT NUMBER NASA/TM-2018-219854		
12. DISTRIBUTION/AVAILABILITY STATEMENT Unclassified-Unlimited Subject Category 37 Availability: NASA STI Information Desk (757-864-9658)					
13. SUPPLEMENTARY NOTES Prepared by the Materials & Processes Laboratory, Engineering Directorate					
14. ABSTRACT This Technical Memorandum explains the friction stir welding process in terms of two basic concepts: the concentration of deformation in a shear surface enveloping the tool and the composition of the overall plastic flow field around the tool from simple flow field components. It is demonstrated how weld structure may be understood and torque, drag, and lateral tool forces may be estimated using these concepts. Some discrepancies between computations and accompanying empirical data are discussed in the text. This work is intended to be helpful to engineers in diagnosing problems and advancing technology.					
15. SUBJECT TERMS friction stir welding, weld process modeling, plastic flow instability, constitutive relations, mechanics of materials					
16. SECURITY CLASSIFICATION OF:			17. LIMITATION OF ABSTRACT	18. NUMBER OF PAGES	19a. NAME OF RESPONSIBLE PERSON
a. REPORT	b. ABSTRACT	c. THIS PAGE			STI Help Desk at email: help@sti.nasa.gov
U	U	U	UU	80	19b. TELEPHONE NUMBER (Include area code) STI Help Desk at: 757-864-9658

National Aeronautics and
Space Administration
IS02
George C. Marshall Space Flight Center
Huntsville, Alabama 35812